RUPRECHT-KARLS-UNIVERSITÄT HEIDELBERG

Klaus Greger

OligoChannel Spectral Analyis in stereotactic laser neurosurgery

Dissertation

HD-KIP-03-18

KIRCHHOFF-INSTITUT FÜR PHYSIK

Dissertation
submitted to the
Combined Faculties for the Natural Sciences and for Mathematics
of the Ruperto-Carola University of Heidelberg, Germany
for the degree of
Doctor of Natural Sciences

presented by

Diplom-Physicist: Klaus Greger
born in: Schwäbisch Gmünd, Germany
Oral examination: 28.5.2003

OligoChannel Spectral Analysis in stereotactic laser neurosurgery

Referees: Prof. Dr. Josef F. Bille
Prof. Dr. Wolfgang Schlegel

Abstract

In stereotactic laser neurosurgery a tumor in the human brain is resected by a pulsed high energy laser beam. The laser beams for diagnosis and ablation of cancerous tissue are supplied through a probe. The whole resection is planned with a computer system. These planning data are based on previously obtained CT and MRT imaging. During the operation the complete process (diagnosis and resection) is guided and controlled by a computer system. One important part of the surgical system is the OligoChannel Spectrum Analyzer (OCSA), of which the principles and development are described in this work. The OCSA analyzes the autofluorescence spectrum of each observed tissue point in order to determine its kind. This is possible since autofluorescence spectra of healthy and cancerous tissue show characteristic differences. In contrast to commonly used techniques, the OCSA uses only a few detectors. By evaluation of the data obtained with the OCSA, an immediate decision can be made whether a specific tissue point should be ablated or not. To demonstrate the new technique, some results obtained with different tissue samples (human kidney and various mouse tissues) will be presented.

Zusammenfassung

In der stereotaktischen Laser-Neurochirurgie soll ein tief sitzender inoperabler Gehirntumor über plasmainduzierte Laser-Ablation entfernt werden. Hierfür werden die Laserstrahlen für Diagnose und Ablation über eine Lasersonde zum Tumor geführt. Die gesamte Operation wird auf CT- und MRT-Daten basierend geplant und durch einen Rechner überwacht. Eine wichtige Komponente des Operationssystems ist der OligoChannel Spektral Analysator (OCSA), dessen Entwicklung und Funktionsweise in der vorliegenden Arbeit vorgestellt werden. Der OCSA teilt Autofluoreszenzspektren untersuchter Gewebepunkte auf einige wenige Kanäle auf, um Aussagen über die Art des untersuchten Gewebes machen zu können. Dies ist möglich, weil die Autofluoreszenzspektren, die durch die Bestrahlung von Gewebe mit Laserlicht entstehen, sich in Abhängigkeit von der Gewebeart charakteristisch unterscheiden. Mit Hilfe der Informationen aus den Autofluoreszenzspektren wird entschieden, wie mit einem analysierten Punkt im Gewebe weiter verfahren werden soll (Ablation, Koagulation oder Verbleib). Zur Demonstration der Funktionsweise dieser neuen Technik werden in der vorliegenden Arbeit auch einige Ergebnisse, die mit Mausgewebe und menschlichem Gewebe erzielt wurden, vorgestellt.

Contents

Abbreviations

5-ALA	5-Aminolevulinic Acid
APD	Avalanche Photo Diode
AO	Adaptive Optics
ASIC	Application Specific Integrated Circuit
CCD	Charge Coupled Device
$ClAlPcS_4$	Chloro-Aluminium phtalocyanine tetrasulfonate
CT	Computer Tomography
cw	continuous wave
EM	Electron Microscopy
HP	Hematoporphyrin
HpD	Hematoporphyrine Derivative
HSS	Hartmann-Shack Sensor
IMRT	Intensity Modulated Radiation Therapy
IR	infrared
LIFS	Light Induced Fluorescence Spectroscopy
MR	Magnetic Resonance
MRI	Magnetic Resonance Imaging
MRT	Magnetic Resonance Tomography
NADH	Nicotinamide Adenine Dinucleotide
OAR	Organ At Risk
OCSA	OligoChannel Spectral Analyzer/Analysis
OMA	Optical Multichannel Analyzer
PDT	Photo Dynamic Therapy
PMT	Photo Multiplier Tube
PpIX	Protoporphyrin IX
ps	picosecond
PSF	Point Spread Function
ReGen	Regenerative Amplifier
SESAM	Semiconductor Saturable Absorber Mirror
UV	ultraviolet

Chapter 1

Introduction

In stereotactic laser neurosurgery tumors in human brains are resected through an optical probe by laser ablation (Fig.1.1) [1, 2]. The probe is guided through the human brain on a predefined pathway. The optimal access to the tumor is determined by matching MRI (Magnetic Resonance Imaging) and CT (Computer Tomography) data obtained prior to the operation [3]. During the ongoing operation, the aim is to find a route to the tumor while causing relatively little damage to vital areas of the brain. The complete operation is done under MRI control. Therefore, the progress of the operation can be evaluated at any time and, if necessary, the strategy for the ongoing operation can be changed, dependent on the current conditions.

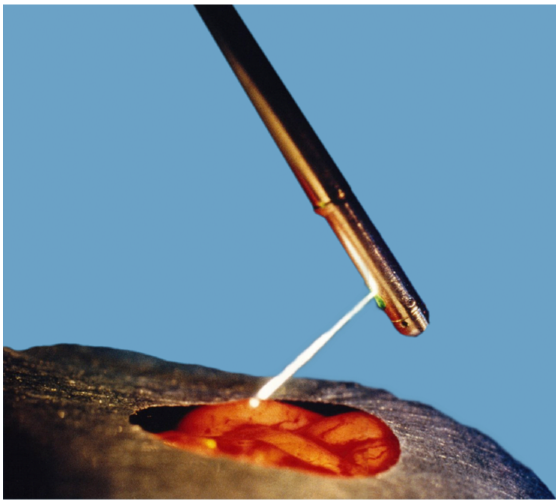

Figure 1.1: The probe tip with laser beam exiting perpendicular to the probe axis.

One serious problem in brain surgery is damage to blood vessels. Due to the minimal invasive access, there is no way of quick intervention if bleeding occurs. Therefore, blood vessels have to be detected with high reliability and closed by coagulation. This coagulation is done by a continuous wave (cw) laser delivering 30 W in the infrared (IR). Besides the MR-monitoring, an integrated confocal microscope is used in order to control the ongoing surgery [4, 5, 6, 7, 8, 9].

During the operation blood vessels, cancerous tissue, and healthy parts of the brain have to be identified. Thus, real time information about the composition of the tissue in each observed sample volume is of major interest. Since the used laser system is working at a pulse repetition rate of about 4 kHz (every single pulse can be switched), the detection system needs to work with at least this frequency. The higher the achieved spatial precision and reliability of detection, the smaller the ablated security regions of healthy tissue can be chosen.

The diagnosis of tissue on biochemical, structural, or physiological levels can be done by measurements with light, like light microscopy, fluorescence microscopy or fluorescence spectroscopy. The spectrum remitted by the tissue sample is influenced by changes in biochemistry and scattering. It is very unlikely that the biochemistry of biological tissue does not change with pathological changes, because every change, like the altered proliferation of tumorous cells is always accompanied by changes in the biochemistry of the cell due to e.g. changed supply conditions. As tissue scattering is usually unspecific to pathological changes, the changes of biochemistry are decoupled from the scattering in a spectroscopic approach.

There are different methods for receiving information about the observed type of tissue by fluorescence. One possibility is the use of fluorescent dyes like 5-ALA (5-aminolevulinic acid) [10, 11, 12], which induces a significantly higher accumulation of PpIX (protoporphyrin IX) in cancerous tissue than in healthy tissue, or $ClAlPcS_4$ (chloro-aluminium phthalocyanine tetrasulfonate) [13], which provide good results in detecting cancerous tissue. The high fluorescence intensity obtained by the use of fluorescent dyes helps finding the exact location of a tumor. Usually, it is then sufficient to measure the complete intensity of the fluorescence signal. The latter is done by only blocking the stimulating wavelength in the spectrum. This method has the advantage of simplicity and high speed. No spectroscopic techniques have to be used. However, the use of fluorescent dyes has some disadvantages. First, applying exogenous material may cause serious side effects, and second, their application is difficult since it is necessary to follow a strict time-table of administration.

The disadvantages of exogenous dyes can be avoided by making use of the autofluorescence properties of tissues. Unfortunately, detection of the overall autofluorescence intensity does not provide sufficient information for reliable identification of different types of tissue. Nonetheless, the shapes of autofluorescence spectra of different tissues contain information which is sufficient for detection of their status (cancer, healthy tissue) [14, 15, 16, 17]. Various tissues have been examined by autofluorescence spectroscopy [18, 19, 20, 21], e.g. skin tissue [22, 23, 24]. It was shown that comparison of the shapes of autofluorescence spectra allows tissue discrimination with high reliability.

A great variety of setups and light sources is used for autofluorescence spectroscopy [25, 26]. In order to access the spectral information, each spectrum has to be analyzed with an Optical Multichannel spectrum Analyzer (OMA). The spectra obtained with OMAs show high spectral resolution but poor sensitivity and speed when CCD devices are used as detectors. Although high signals or long exposure times are required for obtaining spectra, results in literature and

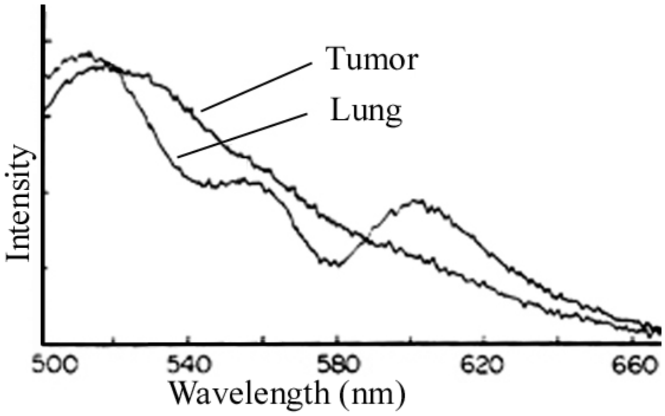

Figure 1.2: Autofluorescence spectra of cancerous and healthy human lung tissue [27]. The excitation wavelength is 488 nm.

our own experiments with a video-based spectrograph show that this procedure is suitable for detection of cancerous tissue [27, 28]. Fig.1.2 shows spectra of healthy and cancerous human lung tissue. There is a clear and characteristic difference between the shapes of the two spectra, which can be used to differentiate between cancerous and healthy tissue. However, it should be mentioned that a working combination of stimulating wavelength and analytic procedure has to be found for each specific application. Excitation with a certain wavelength does not inevitably lead to a characteristic spectral shape.

As long exposure times and high intensities are not available in stereotactic laser neurosurgery, a refined technique had to be found. This is called OligoChannel Spectral Analyzer (OCSA).

In the OCSA, the emitted autofluorescence spectrum of the observed tissue is divided into a few (oligo) spectral bands. The fluorescence intensity is integrated within these bands. By concentrating the whole spectrum on just three detectors, higher signals can be obtained. On the other hand, compared to a simple fluorescence microscope setup with just one detector, information is gained by observing several channels. As shown in the experiments presented later in this work, this information is sufficient for a distinction of different types of tissue. This work describes the development of the OCSA. The principles and methods used for the setup are described. At the end, results obtained with the system, are presented.

A second aspect for the improvement of stereotactic neurosurgery is to evaluate the use of adaptive optics (AO). Adaptive optics is a technique for enhancement of the beam quality in optical systems. It is used for correction of aberrations imprinted on the beams for ablation, coagulation and diagnosis by optical distortions. Such distortions are mainly induced by the biological tissue and irrigation liquid inside the operational cavity that has to be passed by the laser beams. Besides this, some improvement in the optical quality of the optical setup itself can be achieved by adaptive optics.

Adaptive optics is known from its application in astronomy, where it is used to correct aberrations of the signal induced by atmospheric distortions. These distortions are mainly due to turbulences in the atmosphere, which can be described by the model introduced by Kolmogorov in 1961. As the use of adaptive optics is currently just experimental and quite far from an application in the actual stereotactic setup, the principles are described in Appendix A.

In stereotactic neurosurgery, the AO is intended to correct the laser beams for diagnosis, ablations, and coagulation. For diagnosis the use of AO would be helpful in order to collect as much signal as possible from the observed point, because the light levels of the autofluorescence of the human brain tissue are very low. The high energy laser beams, especially those used for ablation, are corrected in order to ensure a good beam quality. This results in a sufficiently small focal point and ensures high intensities for the generation of plasma induced ablation.

Chapter 2

Stereotactic Laser Neurosurgery

Neurosurgical resection and radiotherapy are the standard methods for treatment of tumors in the human brain [29]. Tumors demand additional space in the brain (Fig.2.1), causing increased intracranial pressure. Even with the improvement of the lately developed microsurgical methods, healthy brain tissue is often traumatized during operations. This leads to heavy and often irreversible side effects, like palsy, impaired vision, hearing, and speech or mental disorders. It is difficult or impossible to resect tumors deep in the human brain, because they cannot be accessed without damaging vital areas of the brain.

In radiotherapy, heavy doses of X-ray radiation are applied to the tumor. Usually vital areas of the brain are also affected by the ionizing radiation. Besides this, the necrotic tissue remaining in the head, causes side effects due to its toxic properties.

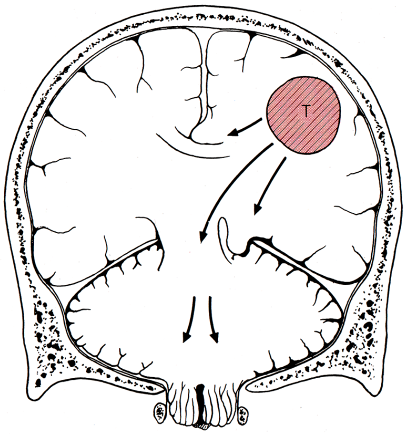

Figure 2.1: A tumor (T) is a space demanding process and causes mass displacements in the brain [30].

These problems are solved by a new approach, the so-called 'laser ablation'. Short laser pulses with time duration of about 30 *ps* lead to plasma-induced ablation of tissue, whereas the surrounding tissue is not affected. The tissue can be ablated gently and very precisely in the 50 μm-range.

Just by using a combination of modern laser technology with the stereotactic approach, i.e. localization, therapy planning and operation procedures, the laser ablation method can play off its advantages (with stereotactic methods a brain area is accessed and treated point by point). On the basis of three-dimensional graphical data, which can be gained with the help of MRI and CT, the position of the tumor within the brain can be determined prior to the operation.

In order to utilize the advantages, namely high accuracy of the ablation process, of this method, a detection system, which analyzes every point in the brain before any action (ablation, coagulation, none) takes place, is included. It is particularly difficult to determine the crossover region from tumorous to healthy brain tissue with the required precision only from the MRI and CT data. Every point has to be closely examined in order to make sure that every cancer cell and a minimum of healthy cells are ablated.

Another serious problem are blood vessels. They have to be determined with high reliability in order not to be injured since this would cause bleedings. Thus, to access low-lying tumors with the laser beam, a guiding system is used. A central part of this system is a scanning probe tip (see chapter 2.2), which can be integrated into an existing stereotactic surgical system. The positioning of the probe in the area of the tumor is done by a stereotactic system. Its coordinates are defined during the initial 3D imaging of localizers prior to the operation (Fig.2.2). The progress of the operation is monitored with a MRI system integrated in the surgical system.

In the first step, the system is used to ablate necrotic tissue killed by radiotherapy. The ablated tissue is removed from the surgical cavity by an irigation/suction unit integrated in the probe. Later on, the method will be applied without prior radiotherapy. Only a low dose irradiation after surgery is planned to kill diffuse infiltrations of tumorous tissue in healthy brain areas.

2.1 Stereotactic Treatment

A stereotactic base ring is invasively fixed to the patient's head (Fig.2.2). This base ring defines an immovable coordinate system relative to the patient's head, the so-called stereotactic coordinate system. Measurement and treatment devices are attached to this ring, so that all coordinates can be uniquely defined relative to the ring. Thereby, tumor areas, organs at risk (OARs) [31], and the optimal access to the tumor can be defined. Thus, an optimal predefined path to the tumor can be chosen with very high accuracy, whereas damages of vital areas can be minimized. The accuracy of this method is in the range of a few tenths of a millimeter.

2.1.1 Stereotactic Radiation Therapy

State of the art in the treatment of non-operable tumors is stereotactic radiotherapy [3]. Planning of the irradiation process is based on CT an MRI data, and the location of the target structures and organs at risk is determined. The X-ray radiation is usually generated by a linear accelerator (Fig.2.3).

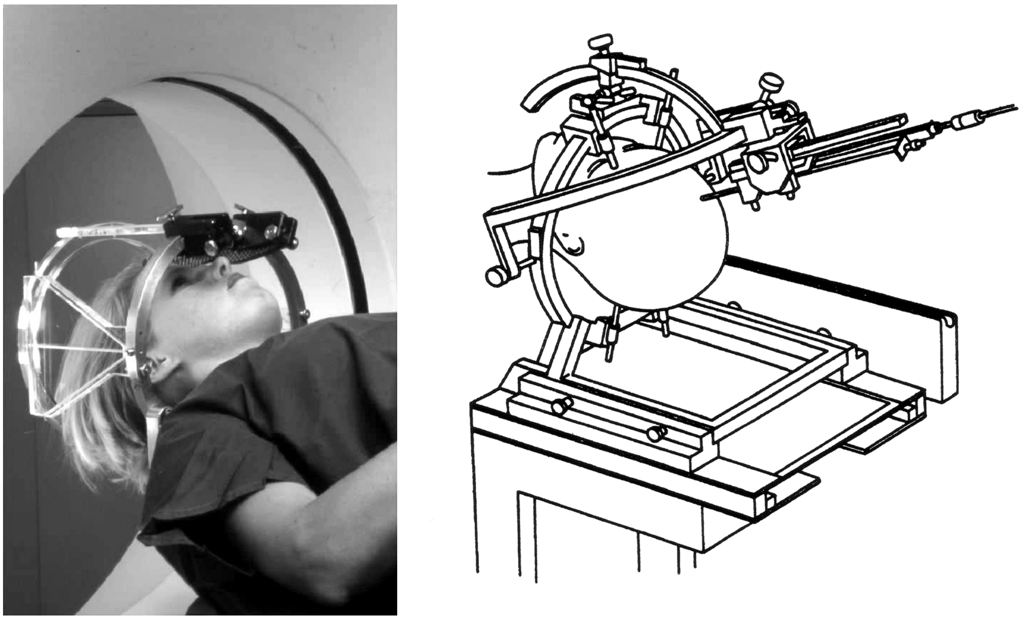

Figure 2.2: left: Patient with stereotactic ring in combination with localizers attached to the head. right: Schematic drawing of a stereotactic system after Riechert/Mundinger. The stereotactic bow mounted to the stereotactic ring fixes the position of the instrument.

2.1.2 Intensity Modulated Radiation Therapy

Figure 2.3: Treatment setup during IMRT. Multi leaf collimator attached to the gantry of a linac.

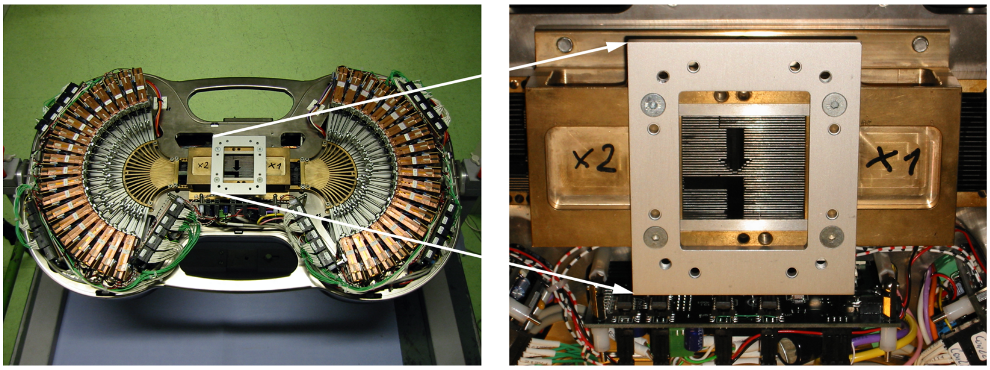

Figure 2.4: Open multi-leaf collimator with detailed view of the lamellas forming the beam.

An enhancement of stereotactic radiation therapy is the Intensity Modulated Radiation Therapy (IMRT). The irradiation field is spatially modulated by a multi-leaf collimator (Fig.2.4). The optimal dose distribution can be ascertained very precisely, ensuring that the dose in the tumor is sufficiently high while the dose in organs at risk is lower than a critical threshold dose. The three dimensional dose gradients can be higher than in conventional radiation therapy. This enables the treatment of tumors lying nearby OARs, like blood vessels or nerves.

2.2 Stereotactic Laser Neurosurgery

As an alternative to the above mentioned methods brain tumors can be treated with laser radiation. On this occasion only thermal processes, which have been used in medicine during the last 30 years, are used for treatment. High energy doses are applied to the tissue, causing denaturation (Nd:YAG-laser) or vaporization (CO_2-laser) of the irradiated tissue. The tissue is not removed by this method, therefore the brain is traumatized due to the high volume of the remaining necrotic tissue. However, laser treatment opens up the possibility of very precise ablation [33].

In Fig.2.5 an overview of the surgical system is given. The high energy laser beams for tissue ablation (5) and coagulation (6) are delivered to the probe (2) by a mirror arm (4). The laser beams are guided to the point of interest in the brain by an optical system, which is assembled inside the probe. The probe itself consists of two tubes which can be moved and rotated. In the inner tube a lens is located which focuses the parallel beam. At the end of the outer tube a deflecting mirror is attached at an angle of 45°. With this setup, by varying the position of lens and mirror, the beam can be focused within a cylindrical volume with diameter and height of about 5 cm each (Fig.2.6) [34].

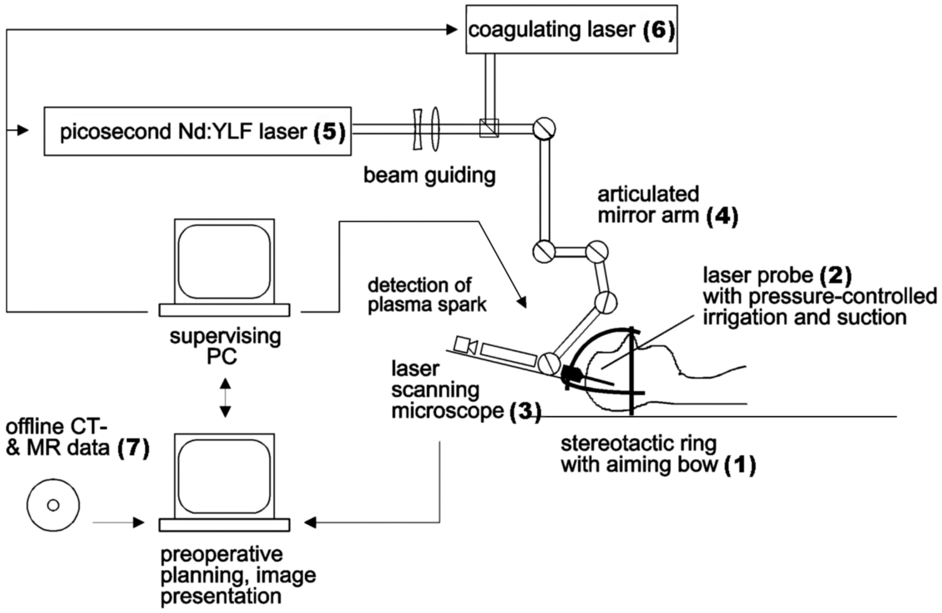

Figure 2.5: Overview of the setup of stereotactic laser neurosurgery. A stereotactic base ring (1) is attached to the patient's head, the laser probe (2) is mounted to the ring and a laser scanning microscope (3) is integrated into the probe for diagnostic purposes. The two high energy lasers (5, 6) for ablation and coagulation are delivered through a mirror arm (4). The surgery is planned based on CT- and MRI-data (7) obtained prior to the operation and the whole system is computer-controlled.

Cancerous tissue is ablated by a picosecond (ps) laser. Its short high energy pulses resect tissue through plasma-induced ablation with high precision (sub-*mm* range), while surrounding tissue is merely unaffected by this process.

2.2.1 The periscopic probe tip

The central part of the stereotactic neurosurgery device is the periscopic probe tip. This is the part of the instrument inserted into the patient's head through a small hole (about 1 *cm*) in the cranium. This instrument consists basically of a lens and a mirror mounted inside of two tubes which can be moved and rotated. A third tube is added around the two inner tubes for the irrigation and suction unit (see below).

The focal length of the lens must not be chosen too small, since this would

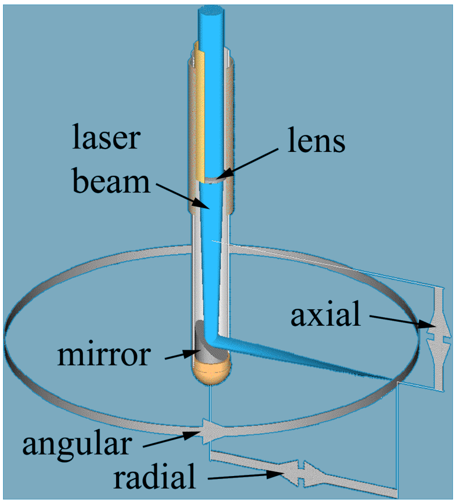

Figure 2.6: Geometry of the periscopic probe tip, the part of the laser probe inserted into the patient's head.

limit the radius of action of the instrument. The lenses used in the instrument have focal lengths of $f = 38\ mm$ and $f = 45\ mm$. In order to get sufficiently small focal spot sizes for ignition of a plasma-induced spark, the diameter of the lens was chosen to 2.8 mm. The lens is mounted at the end of the inner tube of 0.1 mm wall thickness (Fig.2.7). This inner tube has an outer diameter of 3 mm. At the end of the second tube surrounding the first one, a 45° mirror is mounted to deflect the beam by 90° out of the axis of the instrument. By changing the distance between lens and mirror, the distance of the focal point to the instrument's axis is adjusted. By rotating this tube (4.3 mm outer diameter, 0.15 mm wall thickness) the focal point (point of ablation/coagulation) can be rotated around the axis of the instrument. By moving both tubes together the third dimension can be accessed. With this setup a cylindrical volume of 50 mm diameter and 40 mm height can be achieved.

In stereotactic functional neurosurgery very thin needles are used. Their small diameter reduces the risk of damaging upper layers of the brain passed with the instrument. Therefore, the part of the stereotactic laser neurosurgical instrument inserted into the patient's head is designed with small diameter. Unfortunately the smallest achievable size of a focal point w_0 increases with decrease of the input beam diameter w:

$$w_0 = \frac{\lambda f}{\pi w} \tag{2.1}$$

Additionally, the spot size increases with an increase of the focal length f of the used lens.

2.2.2 Irrigation and suction

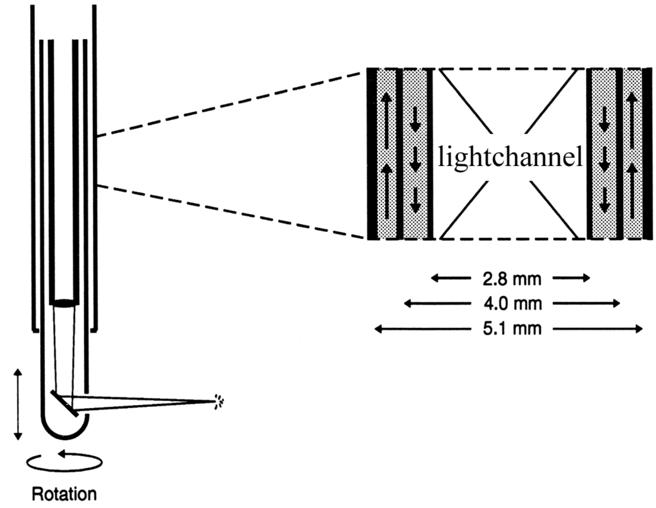

Figure 2.7: Schematic drawing of the tube system used for delivery of the laser light to the tissue in stereotactic laser neurosurgery [35]. The arrows indicate the flow of irrigation liquid in the space between the tubes.

An irrigation and suction unit is integrated into the probe. Between the inner tube (outer diameter 3 mm) and the outer tube (inner diameter 4 mm) irrigation liquid is pumped into the operational cavity. A jet is integrated, so that the liquid is cleaning the mirror constantly. In parallel the liquid passed by the high energy laser beams is changed rapidly in order to avoid thermal lensing effects caused by absorption induced heating of the liquid. Heating would lead to a gradient in the refractive index of the liquid and the beam could not be focused down to the required size. A third tube (5.5 mm outer diameter, 0.2 wall thickness) is added to the system in order to enable the suction of the liquid (Fig.2.7). Therefore 5.5 mm is the outer diameter of the part of the surgical instrument inserted into the patient's head. The irrigation system is equipped with a pressure control. This is necessary because the brain is sensitive to pressure variations [36].

2.2.3 Probe control

The movement of the probe is done with computer controlled stepper motors. Because the motors are very bulky and heavy they are mounted in an external case. The movement is transmitted to the instrument by flexible axles. The step-size of the setup is 2 μm and 0.18° for the rotation. The maximum rotational velocity would be 180 rounds per minute. The actual velocity used for experiments is 30 rounds per minute. The ablation experiments were done with a maximal step frequency of 1.5 kHz.

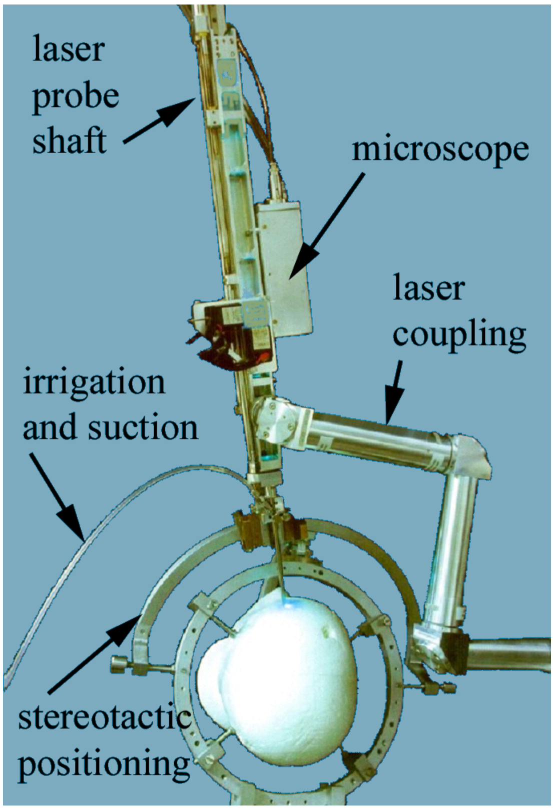

Figure 2.8: Prototype of the stereotactic probe, mounted to a stereotactic system.

2.2.4 Detection unit

In the first design of the laser probe a confocal laser scanning microscope was integrated into the probe (Fig.2.8). The microscope measured the reflected light of each single point and generated an image calculated from these and the position information. The movement of the probe and a scanning movement of the beam acquiring 20 points per probe position were digitized by a computer and displayed, showing the scanned surface. The scanning was done by galvanometric scanners. The detection was achieved by an avalanche photo diode (APD). As a point-source an argon laser emitting 25 mW was used. The laser light was coupled into an optical fiber and transmitted to the probe. This confocal microscope was assigned for the detection of the blood vessels. The detection of blood vessels is of great importance in order to avoid their damage during surgery. Due to the minimal invasive access of the method a quick interaction is not possible without opening the head of the patient. Therefore, it is important to detect vessels and close them by coagulation before they are ablated. The obtained images did not show the blood vessels with the required reliability, because the intensity signal of a confocal microscope strongly depends on focusing conditions. Thus, a refined detection is required.

Another reason for the requirement of a refined detection mechanism is the fact that the precision of the setup cannot be exploited by just using MRI or CT data. The resolution of these methods is limited to an order of mm. The precision of ablation, in contrary, is in the range of 50 μm. A detailed analysis of the tissue during surgery would increase precision and therefore minimize harm to the patient, because the security region ablated around the actual tumor could be minimized. This is impossible with a simple reflective confocal microscope, because the signal is affected by several influences like attenuation by tissue in the optical pathway, debris on the optics or out-of-focus conditions.

Previous experiments with a confocal fluorescence microscope were done by M. Zenzinger et al. [37]. With this setup, detection of cancerous tissue using fluorescent dyes was possible. The overall fluorescence signal was measured without using spectroscopic techniques. Blood vessels were not taken into consideration. However, due to the special fluorescence characteristics of blood, additional detection of blood vessels is likely to be possible with the stereotactic setup.

In this work, a completely new approach is presented. Detection and discrimination of tissue types is done by making use of autofluorescence spectroscopy. The complete spectrum emitted by the tissue is taken into account. Since different tissue types have characteristic autofluorescence spectra, each spectrum contains much more information than the overall fluorescence intensity detected by the devices described above.

Chapter 3

Fluorescence

The ability to spectrally analyze and spatially resolve absorption and fluorescence signals allows two different tasks. First, it can provide information for detection and monitoring of physiological states of tissues, including disease; second, it can lead to functional imaging. In functional imaging a property (metabolic state, type of tissue) of the specimen is displayed, not just an optic property (reflectance, fluorescence intensity). Imaging in tissue is always degraded by the strong optical scattering in biological tissue. Thus, any imaging technique must discriminate in favor of the unscattered "ballistic" light signal (which is usually extremely weak). A good possibility is the use of spectroscopic techniques, as the spectrum of the emitted light is merely affected by scattering.

A tumor causing clinical symptoms is normally large enough to be localized by conventional methods like X-ray imaging, CT, MRI, palpation or endoscopy. As the chance to treat a tumor decreases with time, an reliable detection of early-stage lesions is needed. These early stages of malignant tumors are often not accessible by conventional techniques. For many kinds of cancer there is no reliable detection method available. For example, small papillary lesions in the bladder are difficult to detect by white light cystoscopy. This requires random tissue biopsy in order to test for preexisting or recurrent diseases after treatment. These problems and the improvement of new light sources (especially lasers), optical fibers, medical endoscopes, and detectors led to the development and evaluation of fluorescence spectroscopy and imaging for detection, staging or characterization of malignant and premalignant lesions. The likelihood for successful treatment and reduced complications can be significantly increased if primary and recurrent tumors can be detected at early stages. The concept of optical biopsy helps finding lesions by optical measurements while no removal of tissue is needed. If the premalignant sites cannot be found directly, it may help find suspicious sites for biopsy. Advantages of the spectroscopic method are the sensitivity, especially for point measurements, the suitability for tissue surfaces and the applicability in a minimal invasive surgery environment.

In vivo and *ex vivo* characterization of biological samples by fluorescence imaging and fluorescence spectroscopy has been well established over several decades [38, 39]. The method is based on the localization of fluorophores (fluorescent molecules) in tissue and cell structures. Fluorescence microscopy is routinely used for histology [7, 40]. *In vivo* techniques are, for example, used for the guidance of surgical resections. The first studies using Light Induced Fluorescence Spectroscopy (LIFS) were conducted by Policard et al. in 1924, reporting fluorescence (attributed to endogenous porphyrins) of tumors illuminated with UV/violet light. In 1942 Auler et al., Banzer et al., and Figge et al. reported red fluorescence after giving exogenous porphyrins to animal tumors. Moore was the first to report improved detection of brain tumors *in vivo* with the use of fluorescin. The problems with exogenous dyes, like photosensitized skin, and independent developments in autofluorescence spectroscopy induced further research on spectroscopy. The goal of this research was to characterize tissue by using the spectral information from endogenous dyes. Pioneer work on this field was done by the groups of Protio, Alfano [41] and Yang with *in vitro* and *in vivo* studies on human and animal tumor autofluorescence.

Kriegmair et al. proposed the use of 5-ALA-induced PpIX fluorescence for diagnosis in the bladder [42]. *In vivo* fluorescence techniques had significant impact on the development of Photo Dynamic Therapy (PDT) treatment. Visualization plays an important role in the development of PDT, because of the ability of getting direct information on the pharmacokinetics of the photosensitizers by monitoring their uptake and photobleaching.

There is an increased interest in fluorescence-based techniques in oncological applications in order to detect and characterize premalignant or malignant lesions by *in vivo* fluorescence spectroscopy and imaging. Several papers have already reviewed several aspects in this field. Richard-Kortum and Sevick-Muraca [14] have discussed several spectroscopic methods, including fluorescence, from a quantitative point of view. B.C. Wilson described oncological *in vivo* applications of fluorescence spectroscopy, which were classified according to the type of fluorophores and the used instrumentation [43]. One classification is done in terms of the light detection scheme and the used light source. One type of light detectors are time gated and/or time resolved detectors using light pulses or cw (continuous wave) devices.

In cells, various numbers of fluorescent dyes are present, providing information about the biochemistry of the cell. For a single photon-activated compound the fluorescence intensity I_m follows a monoexponential decay with time t resulting from an impulse of incident light.

$$I_m(t) = I_0 \frac{\epsilon\alpha(C(r))}{\tau} L \exp\left(-\frac{t}{\tau}\right) \tag{3.1}$$

I_0 is the incident intensity, ϵ the extinction coefficient of the fluorophore at the excitation wavelength, (C(r)) the concentration of the sample, α the quantum yield at the emission wavelength, τ the lifetime of the sample and L the distance covered in solution. The lifetime τ is the mean time between the absorption of an extinction photon and the remission of a fluorescent photon.

The steady state intensity is obtained by integrating over all remission times.

$$I_m = \int_0^\infty I_0 \frac{\epsilon\alpha(C(r))}{\tau} L \exp\left(-\frac{t}{\tau}\right) = I_0\epsilon\alpha(C(r))L \tag{3.2}$$

This is a simple function dependent on the sample concentration, absorption coefficient, and quantum yield. The remitted intensity is determined by the environment of the sample which has an impact on the extinction coefficient ϵ and the quantum yield α, and the local concentration. Intensity measurements are affected by the attenuation of excitation and fluorescent light while propagating in tissue. In the presented experiments, the absolute intensity information is suppressed by simply using relative intensities.

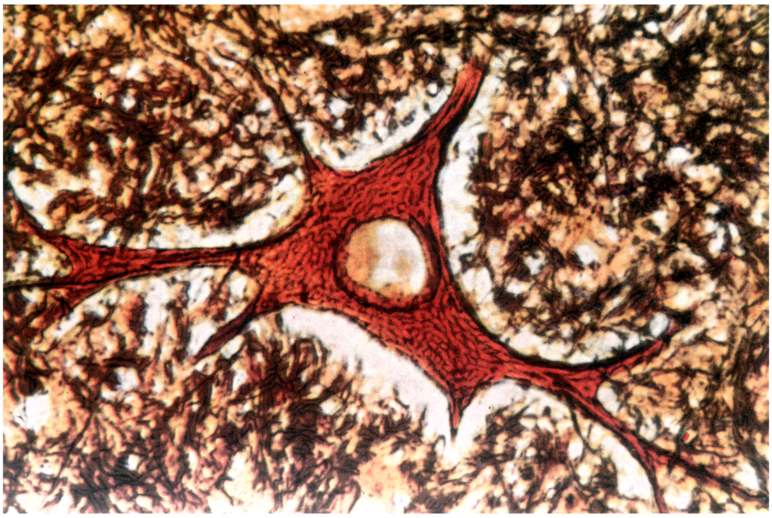

Figure 3.1: Multipolar nerve cell stained with pyridin-silver-goldchlorine [44].

While looking at biological samples, the imaging quality is often limited by the lack of contrast, not by poor resolution. A classical method of gaining contrast and information is the use of dyes, which stain the different parts of the sample in different ways (Fig.3.1). In pathology, the sample is cut into very thin slices and stained with different types of dyes. Thus, the sample is seen in different colors, due to the changed reflective properties of the sample. This method is applicable only in fixed tissue, not *in vivo*.

Fluorescent dyes work slightly different. In the case of fluorescent dyes, the dye emits light in a characteristic manner, i.e. the emiting wavelength differs from the wavelength of absorbed light. The molecules of exogenous or endogenous dyes in biological samples are soluble macromolecules in the cell. In the first step a molecule absorbs the energy $E = h\nu'$ of a photon. Typically, the molecule gets excited from its ground energy level $S_{0,0}$ to the first excited state $S_{1,v}$ (Fig.3.2). By inner conversion, the molecule relaxes into the $S_{1,0}$ state. This state has a lifetime of the order of $10^{-9}s$. A photon is emitted by the molecule, transiting from the excited to the ground state. The energy $h\nu$ of the emitted photon is lower than the energy of the absorbed photon ($\nu < \nu'$). In fluorescence microscopy this

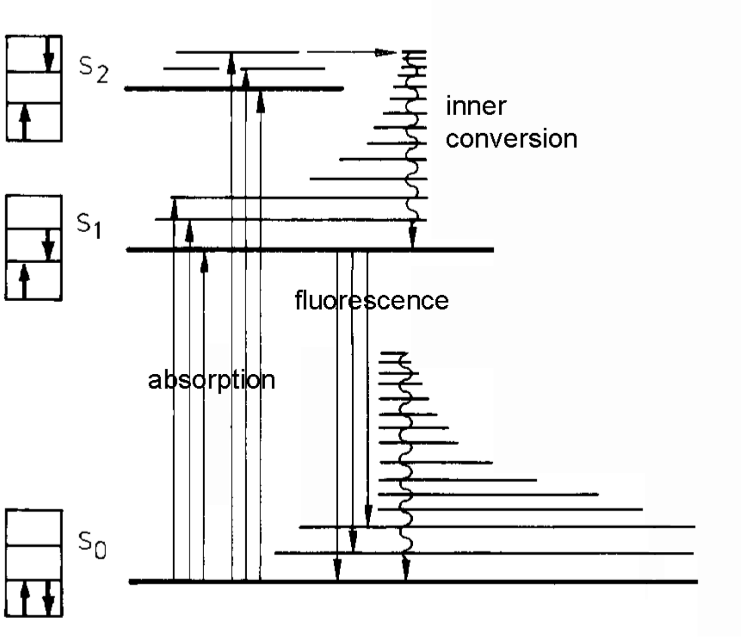

Figure 3.2: Typical term scheme of a molecule.

property is used to separate the exciting light (in our case from a laser), which illuminates the sample, from the light emitted by the observed tissue sample. An edge filter or, as in our setup, a dicroic mirror can be used. The edge filter absorbs light higher/lower than a certain frequency. The dicroic mirror consists of a dielectric coating reflecting light with the frequency of the laser and transmitting the remaining frequencies. With this setup it is possible to separate the exciting frequency from the light for analysis.

There are different types of fluorescence dyes (fluorophores):

- Exogenous dyes
- Fluorophore precursors
- Endogenous fluorescence dyes

Each of these classes of fluorophores has distinct limitations and advantages for different applications.

3.1 Exogenous fluorescence dyes

In the 1950s, the accumulation of HP (hematoporphyrin) in various types of cancer was reported. From this, HpD (hematoporphyrin derivative) was developed for the localization of cancer in various organs, including esophagus and cervix [45] and for the characterization of suspicious head and neck lesions. Some of these early studies were very successful in observing cancer in an advanced stage. Current work focusing on early stage cancer and premalignant lesions is not that successful. The early studies were conducted under direct-viewing conditions. Dorion and Kinsey therefore used photoelectronic detectors in order to gain sensitivity. Based on their work, many other studies using fluorescence diagnostics were conducted. As most of the exogenous dyes have been initially developed for the use as photosensitizers for Photo-Dynamic Therapy (PDT), they do not yield optimum results in fluorescence diagnostics. The selectivity of these fluorophores initially developed for PDT is rather poor. Lam et al. [46] found by stepwise decrease of the dose of HpD (they tried to reduce the photosensitivity of the skin) that early lesions could be detected with high accuracy with the detection of autofluorescence.

In the work presented here, only the autofluorescence of the observed tissue was used. It was possible to confirm the suitability of the method proposed by Lam et al. for detection of different types of tissue. However, for the monitoring of the concentrations of the photosensitizer agents in PDT, the exogenous dyes can be very helpful. Improved results might be achieved with a combination of exogenous and endogenous dyes compared to just using one of the methods.

Exogenous dyes can be administered to the patient e.g. by injection or oral. There are various advantages of exogenous dyes. The photo-physical properties can be selected and are well known. Thus, the pharmacokinetics can, in principle, be chosen to optimize targeting. Another advantage is that the fluorescence signal intensity can be much higher compared to autofluorescence, which simplifies instrumentation. Exogenous dyes can have different properties which can be used for diagnosis. Some dyes concentrate in cancerous tissues due to the changed metabolism in cancerous cells. The transport of educts is impaired in cancerous cells. This higher concentration of dyes can be used to recognize cancerous tissue. An important question in the context of fluorophores is why they localize more or less selectively in tumors. Knowledge about the mechanisms of enrichment would enable the development of optimized fluorophores. Another mechanism responsible for higher concentrations of fluorophores in tumor tissue is that the quality of blood vessels in tumors is poor and the vessels are leaky, leading to an early release of systemically administered drugs through the vascular wall. In combination with a poor lymphatic drain this leads to a higher uptake and retention of fluorophores. One of the main disadvantage of exogenous dyes is that their handling is difficult. Normally a very strict time-table has to be followed in order to obtain good results. The main drawback of exogenous dyes are the side effects. For example, dyes (e.g. acridin orange [4]) that bind to the DNA are not applicable *in vivo* due to their carcinogenic potential. *In vitro* very good results can be achieved. Therefore they can be used for the characterization of tissue samples obtained in a biopsy.

3.2 Fluorophore precursors

Fluorophore precursors are substances inducing the production of fluorescent dyes in the cell. 5-ALA (5-aminolevulinic acid) for example induces the production of PpIX (protoporphyrin IX) in the cell. 5-ALA is a precursor in heme biosynthesis, introducing a corresponding increase in heme biosynthesis. The penultimate step in this synthesis is the fluorophore PpIX. The last step in heme synthesis is the incorporation of iron into PpIX and takes place under the action of the enzyme ferrochelatase in mitochondria. In tumors, the activity of this enzyme is lowered/reduced and therefore the penultimate product PpIX is enriched [47, 48]. Another factor for tumor selectivity is the low penetrability of 5-ALA through intact skin and cell membranes due to its hydrophilic property. In contrast, skin tumors have an increased permeability of, leading to a higher concentration of 5-ALA in the tumor when applied locally. As this is an effective photodynamic sensitizer it was primarily used in photodynamic therapy (PDT). Photodynamic therapy involves the systemic administration of a photosensitizer that visualizes tumors and its subsequent activation by light of an appropriate wavelength. This induces photochemical reactions which cause photodamage to the tumor. The use of 5-ALA for PDT treatment has been reviewed by Peng et al., who also summarized the clinical and developmental status of fluorescence diagnosis with 5-ALA [49]. The concentration of PpIX induced endogenously from exogenous 5-ALA in tumors reaches its maximum from one to six hours after systemic administration of 5-ALA. During subsequent investigation, the applicability of fluorescence detection and localization of dysplasia and early stage cancer has been investigated. The contrast caused by PpIX depends on several pharmacological and physiological factors that can alter the distribution and kinetics, the local rate of heme biosynthesis and the rate of clearance of PpIX [50]. The mechanisms of the accumulation of porphyrins in tumors is not clear yet. Even in the same patient, the contrast can vary with time and from lesion to lesion. Varying concentration in premalignant and malignant tissues may be traced back to differences in the cell or the changed micro-environment. It can be administered oral or intravenous, while topological application or instillation can be used in dermatology or in hollow organs like the bladder. Typically, the period of time from a single dose application to peak fluorescence is about seven hours. The peak ratios of tumor to normal tissue are in the order of 10:1 [51]. The 5-ALA-induced PpIX fluorescence increases and decreases faster in tumor tissue than in normal tissue. Therefore the time of observation is very important. The specific PpIX distributions inside a cell have to be taken into account. Certain variations of 5-ALA (e.g. lipophilic derivatives for increased tissue penetration) are used in order to modify the distribution of PpIX in the tissue.

3.3 Endogenous fluorescence dyes - Autofluorescence

Endogenous fluorescence dyes are responsible for the autofluorescence of tissue. Transitions between energy levels of molecules intrinsic to the tissue are excited and the emission is detected. The main advantage of endogenous fluorophores is the lack of side effects since only substances intrinsic to the cell are used. The tissue observed *in vivo* is not affected. The disadvantages of autofluorescence are the low light levels compared to the use of exogenous dyes. But this problem/drawback can be solved by refining the used detection technique. In principle, there is enough information in the autofluorescence signal for characterization of the tissue.

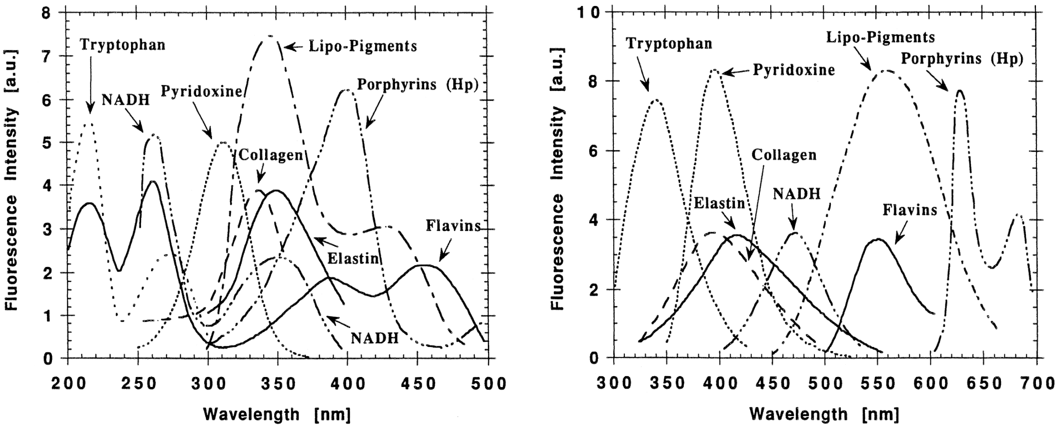

Figure 3.3: Absorption (left) and emission (right) spectra of several substances in a cell [43].

The most frequent molecules of a cell are either located in the structural matrix of the cell or part of the cell metabolism. The most important fluorophores in the cell matrix are collagen and elastin, the fluorescence of which is a result of cross-linking between amino-acids [14]. Flavin and the reduced form of nicotinamide adenine dinucleotide (NADH, only the reduced form is fluorescent) are the fluorophores involved in the metabolism. Other fluorophores are aromatic amino acids (tryptophan, tyrosine, phenylalanine), porphyrins and lipopigments (ceroids, lipofuscin) that are the endproducts of lipid metabolism. In addition, red porphyrin fluorescence due to bacteria may be detectable in certain body sites (not the brain) and lesions. Fig.3.3 shows the excitation and emission spectra of various endogenous tissue fluorophores. Any given tissue contains a characteristic mixture of fluorophores. As in cancerous tissue the concentration varies compared to normal tissue, the autofluorescence properties can be used to detect cancer.

The characteristics of tissue depend on the following points:

- Each fluorophore has special excitation and emission characteristics.
- A given tissue contains a mixture of various fluorophores in different concentrations.
- The distribution of the fluorophore concentrations is not constant in tissue. Especially it varies with depth in the tissue due to the layered structure (e.g. mucosa, submucosa, muscularis). Each of these layers has a different fluorophore composition. Optical sectioning (with a confocal setup) has to be used to separate the layers and to suppress signals from other layers.

The detectable changes of fluorescence signals in cancer tissue due to metabolic or morphological changes vary with the used wavelengths for excitation and detection. The autofluorescence of premalignant lesions or early cancer can alter some tissue characteristics:

- The concentration and spatial distribution of fluorophores.
- The metabolic status of the cell and the fluorophore (e.g. only the reduced form of NADH is fluorescent).
- The biochemical and biophysical environment of the tissue. This can alter quantum yield, position of the spectral peaks and the width of the peaks.
- The tissue structure, like mucosal thickening or the complete loss of layered structure.
- The altered concentration and distribution of hemoglobin and other chromophores changes the wavelength-dependent attenuation.

The alteration of these signals by metabolic and structural changes influences the excitation and emission wavelengths of the examined fluorophores. For a given application, a working combination of excitation and detection wavelengths has to be found. Some fluorophores (e.g. aromatic amino acids of proteins) can only be observed in the UV range, while others can be excited with visible light. The depth penetration increases with wavelength and has its maximum (therapeutic window) in the infrared (700-1100 nm). For each application or body site there may be one or more optimal combinations of excitation and emission wavelengths. These are generally not known and thus have to be determined. This optimization can be done *ex vivo* with tissue biopsies or *in vivo*. The *ex vivo* optimization has the advantage of refined spectroscopic and microscopic devices but the spectra might be changed due to altered metabolic status or the lack of blood supply.

Chapter 4

Materials and Methods

4.1 Spectrograph

For our preliminary experiments [28] and the OCSA applications, a spectrograph based on a prism (the dispersion of the prism) was applied. Fig.4.1 shows the general setup of such a spectrograph. On the left, a pinhole generates a spot of light; in our setup this is realized by a pinhole onto which the beam from the probe is focused. The light is collimated by an achromatic lens (lens 1). Behind the prism the beam is focused onto the screen/detector by a second achromatic lens (lens 2).

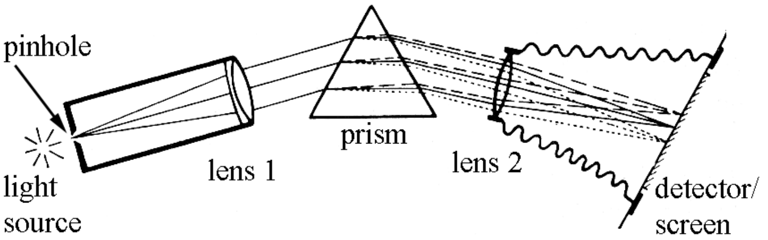

Figure 4.1: Schematic drawing of the spectrograph. The light from a point source (light source with pinhole) is collimated onto the prism. Behind the prism the beam is refocused onto the screen [52].

The central part of the spectroscopic device, the OligoChannel Spectral Analyzer (OCSA, see chapter 5), is a prism. Light that crosses a prism is deflected by an angle δ. Here, the symmetric transition of a beam is described, that means that $\alpha_1 = \alpha'_1$ and $\alpha_2 = \alpha'_2$. In this case, δ is minimal and the following relation is fulfilled:

$$\gamma + \delta = 2\alpha \tag{4.1}$$

With the law of refraction the result is:

$$\frac{\sin\alpha_1}{\sin\alpha_2} = n = \frac{\sin(\gamma+\delta)/2}{\sin\gamma/2} \tag{4.2}$$

or:

$$\sin\frac{\gamma+\delta}{2} = n\sin\frac{\gamma}{2} \tag{4.3}$$

The refractive index n is dependent on the wavelength of the light. Thus, different wavelengths are refracted in different angles. This is called dispersion. According to equation 4.3 the angle of deflection is dependent on the refractive index $n = n(\lambda)$. A beam of light consistent of different wavelengths can be separated into its spectral components. In our experiments, a prism with a

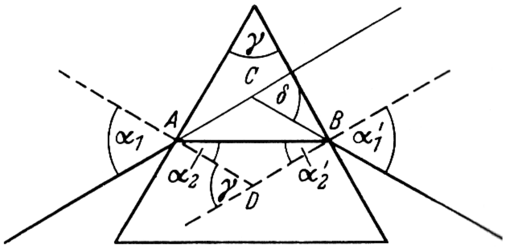

Figure 4.2: Deflection of light transmitting a prism. The symmetric case is shown.

dispersion of 3° between $\lambda_1 = 480\ nm$ and $\lambda_2 = 643.8\ nm$ was used. With the used focusing lens, which had a focal length of 120 mm, an incident angular deflection of three degrees (corresponding to a wavelength divergence of 163.8 nm) leads to a beam displacement of 6.3 mm on the detection screen. A wavelength divergence of 50 nm (which was used in our experiments) results in a displacement of 1.9 mm on the screen.

4.2 Beam expander

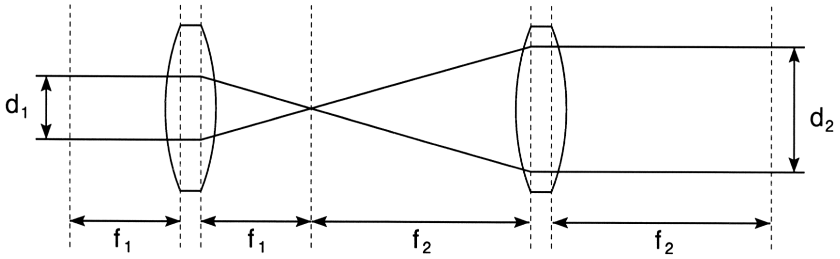

Figure 4.3: Transformation of beam diameter and scanning diameter by a telescope [53].

Beams often have to be transformed to another diameter in optical setups, e.g. in adaptive optics (AO) setup described in Appendix A, the sizes of the wavefront sensor and the deformable mirror are not the same. In addition, the optical elements (wavefront sensor, deformable mirror and the distortion itself) of the AO system have to be in optically conjugated planes. These are planes in which beams have equal properties. A parallel beam in one conjugated plane is parallel in all other conjugated planes. A focal point is transformed to another focal point, and wavefronts are of the same shape in all conjugated planes. A pupil can be transformed by an afocal or 4-f-system from one to another conjugated

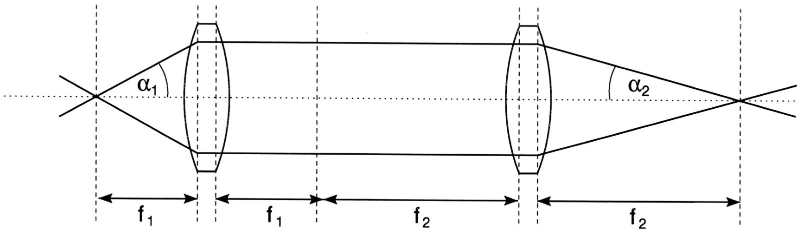

Figure 4.4: Transformation of beam angles by a telescope.

plane. Two lenses are arranged at a distance of $d = f_1 + f_2$ to form a telescope. Beam diameter (Fig.4.3) and angle (Fig.4.4) are transformed as follows:

$$d_2 = d_1 \frac{f_2}{f_1} \tag{4.4}$$

$$\alpha_2 = \arctan\left(\frac{f_1}{f_2}\tan\alpha_1\right) \tag{4.5}$$

For small angles this can be approximated:

$$\alpha_2 = \frac{f_1}{f_2}\alpha_1 \tag{4.6}$$

4.3 Confocal Microscopy

The tissue is observed by a confocal laser scanning microscope [5] integrated in the probe [37, 54].

Fig.4.5(a) shows the setup a conventional microscope. The whole object plane is illuminated and imaged onto the image plane. The optical quality of the illuminating lens (condenser) is of minor importance for the quality of the image, since the quality of the image is mainly defined by the quality of the objective (imaging lens). Fig.4.5(b) and 4.5(c) show setups of scanning microscopes. In the first case (b) the completely illuminated object is imaged by a point detector that scans the image plane. In the second case (c) the object is illuminated by a small spot (point source) and the whole intensity in the image plane is detected. The scanning microscopes have the advantage of an adjustable size of the imaged region. Due to the serial acquisition of the data, the data can easily be recorded by a computer. Electronic image enhancement algorithms can be used. The imaging properties of the three microscope types ((a), (b), and (c)) are the same.

Compared to conventional setups the confocal system has improved imaging properties [6]. A general setup of a confocal microscope is shown in (Fig.4.5(d)).

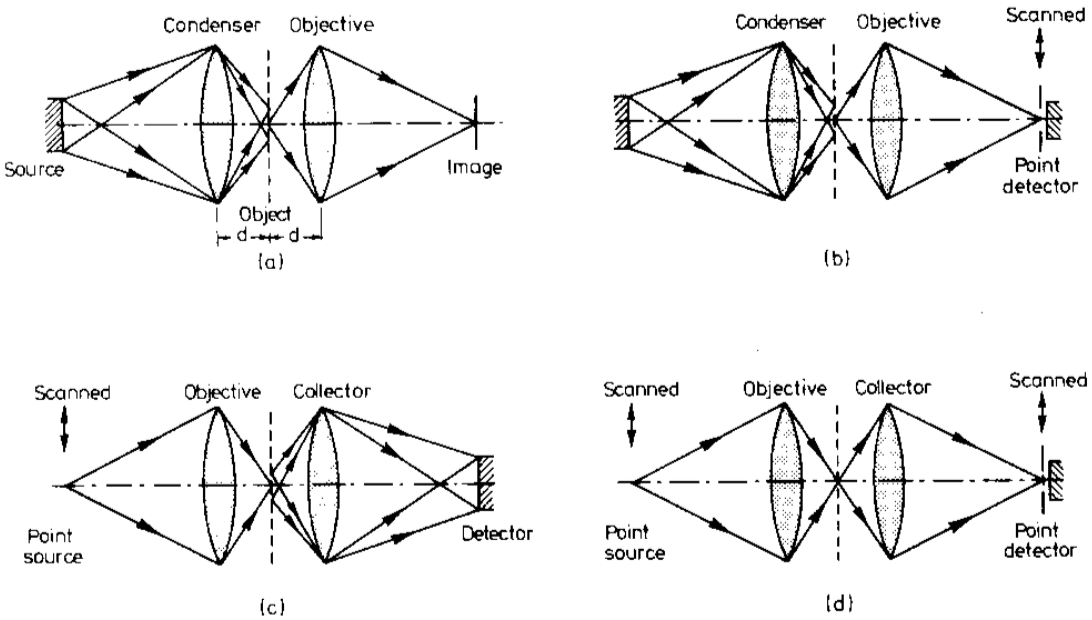

Figure 4.5: Different types of microscopes: (a) conventional microscope; (b), (c) different types of conventional scanning microscopes; (d) confocal microscope [5].

The confocal microscope uses a point source *and* a point detector. In reflection mode (Fig.4.8) one lens is used for point illumination and point detection. The advantages of this setup is, that it is self-aligning.

The resolution of a conventional microscope is defined by the diffraction of the lens. Imaging a point by a lens the the point spread function is an airy-disk (Fig.4.6):

$$I(v) = I(0)\left(\frac{2J_1(v)}{v}\right)^2 \tag{4.7}$$

J_1 is the first Bessel function. With $\sin\alpha$, the numerical aperture we get for v:

$$v = \frac{2\pi}{\lambda} r \sin\alpha \tag{4.8}$$

In the confocal setup the point spread function is squared, because the lens is used twice, first for imaging of the point source onto the observe point, and second for imaging of this illuminated point onto the point detector. This leads to the following function:

$$I(v) = I(0)\left(\frac{2J_1(v)}{v}\right)^4 \tag{4.9}$$

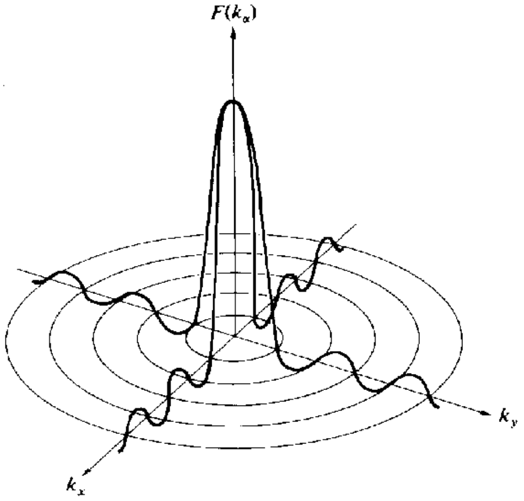

Figure 4.6: Airy disk.

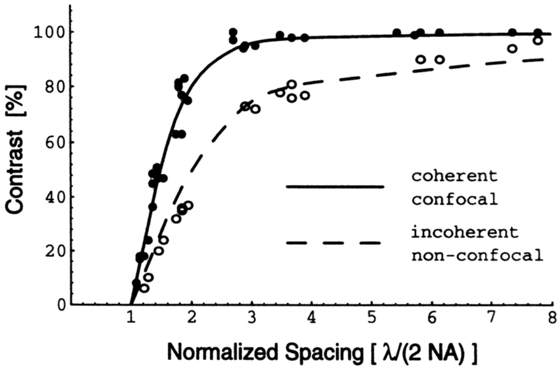

Figure 4.7: Experimental contrast transfer values as a function of the spatial period of a line grating [7].

Fig.4.7 shows, that the ultimate resolution of a confocal scanning microscope in reflection mode and a conventional microscope are the same, but the contrast produced by a confocal microscope is higher. For very small pinholes (smaller than the airy disk produced by a point fluorescent object) and fluorescence imaging, the resolution of a confocal microscope can increase by a factor of $\sqrt{2}$.

4.3.1 Sectioning

One of the main advantages of a confocal microscope is its optical sectioning capability. This means that only light from the focal point (Fig.4.8 solid lines) is able to enter the point detector. Light from other than the focal spot (Fig.4.8 dotted lines) is not focused onto the point detector and does not contribute to the signal since they are rejected. This is a very important property for our purposes, as there are many disturbing influences in the operational cavity (plasma sparks, debris in the path of light), which have to be discriminated in order to obtain an interpretable signal.

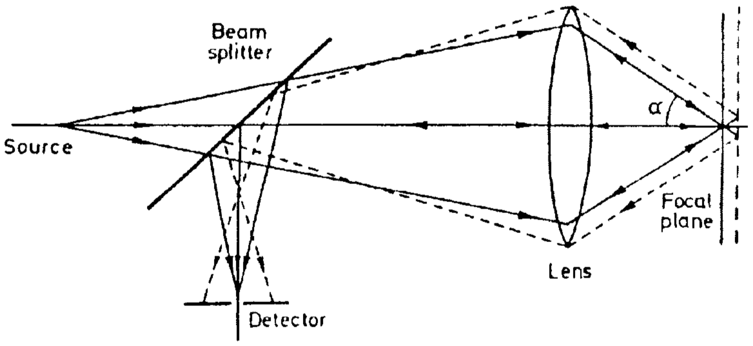

Figure 4.8: Sectioning properties of a confocal microscope [7].

The intensity along the optical axis of the illumination point is:

$$I(u) = \left(\frac{sin(u/4)}{u/4}\right)^2 I_0 \tag{4.10}$$

with:

$$u = \frac{2\pi}{\lambda}\left(\frac{a}{f}\right)^2 z \tag{4.11}$$

Fig.4.9 shows the depth resolution functions dependent on u for conventional and confocal microscopes. In a conventional microscope (dotted line) the reflected intensity of a point reflector is proportional to the intensity at this point and therefore proportional to function 4.10. The depth resolution is given by the width of the function at half maximum intensity $I_{1/2} = I(u_{1/2}) = 1/2I_0$. Solving the equation 4.10 gives a value $u_{1/2} = 5.566$. With equation 4.11 a value for the depth resolution can be calculated from focal length f of the lens and the beam diameter a:

$$z_{1/2} = \frac{2\lambda}{\pi}\left(\frac{f}{a}\right)^2 u_{1/2} \tag{4.12}$$

In a confocal microscope the illumination focus is imaged onto the detection pinhole. The depth transfer function is displayed in Fig.4.9 as a solid line. By the additional imaging of the illuminated point the point spread function is squared. This leads to the depth transfer function of the confocal microscope:

$$I(u) = \left(\frac{sin(u/4)}{u/4}\right)^4 I_0 \tag{4.13}$$

u is defined in equation 4.11. In this case, the width at half maximum is $u_{1/2} = 4.008$. The depth resolution is improved by a factor of 1.39. These are the calculations for the transfer function of a single point. For a three-dimensional object, the differences are bigger because the neighboring points have to be taken into account. In the case of a conventional microscope, the same brightness is detected from out-of-focus points as from objects in the focus. However, the light from out-of-focus points does not carry information. If for example a mirror is moved along the optical axis (the distance to the lens is changed), the detected intensity does not change with distance.

In contrast, the confocal microscope works different. As in the case of the mirror there is only light from the focal point detected. Signal can only arrive at the detector if the mirror is in the focal plane. Light from outside the focal point is rejected. This is an important property for detection of the spectrum of a single point in the human brain, surrounded by other points emitting or reflecting light.

In order to reach even better suppression of disturbing signals the use of two-photon microscopic/spectroscopic technique is possible. In two-photon spectroscopy a short pulsed laser is used for excitation. Thus, very high intensities are reached. With these very high intensities it is possible to excite energy levels with the energy of two photons. As the excitation probability increases quadratic with intensity, in two-photon spectroscopy the Point Spread Function (PSF) is further improved compared to normal microscopy. The excitation wavelength can be filtered very easily because the emitted photons have higher (up to twice as much) energy than the excitation wavelength. Confocal and two-photon microscopy can be combined in order to further increase the PSF and suppression of disturbances.

4.4 Laser-Tissue interaction

Interaction between tissue and laser can be characterized by the mode of operation. Dependent on the intensity of the laser and the duration of the interaction,

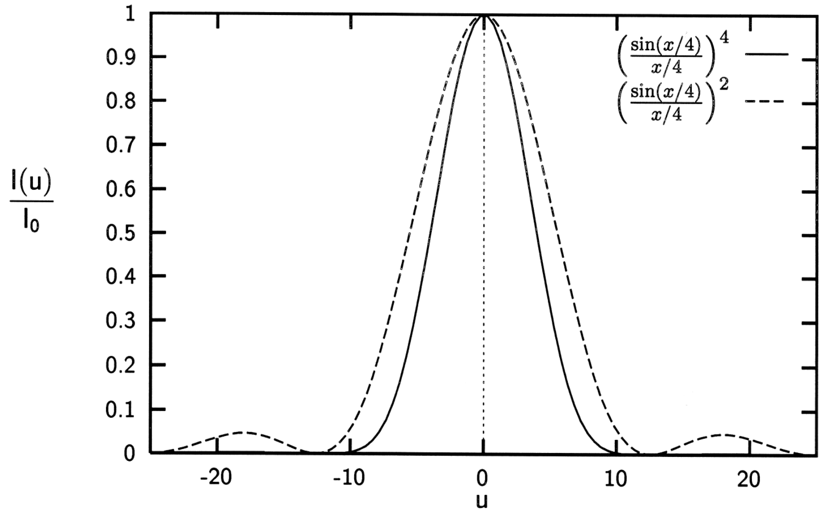

Figure 4.9: Depth resolution of a confocal (solid line) and a conventional (dotted line) microscope [7].

different types of laser-tissue interactions are distinguished [55, 56]: chemical, thermal, photo-disruptive or plasma-induced interactions (Fig.4.10). For stereotactic laser neurosurgery plasma-induced laser ablation by a picosecond laser is used.

4.4.1 Photo-chemical interaction

For photo-chemical interaction of light with tissue the presence of an exogenous substance, a photosensitizer is needed. This is a substance (e.g. Hematoporphyrin derivative (HpD)) that develops its toxic properties after irradiation with light of a certain wavelength. The main advantage of this Photo-Dynamic Therapy (PDT) is that diffusely growing tumor cells can be accessed and destroyed, because the used photosensitizers accumulates in tumorous tissue selectively. Photochemical interactions take place at very low power densities (typically 1 W/cm^2).

4.4.2 Thermal interaction

The thermal interaction of light with tissue is based on simple heating of the irradiated volume. The electro-magnetic energy is transformed to heat by excitation of the vibronic and rotatory states of the molecules. The excited molecules transfer their energy into heat by inelastic scattering with neighboring molecules. Pulsed lasers and lasers emitting continuous waves can be used (typical pulse

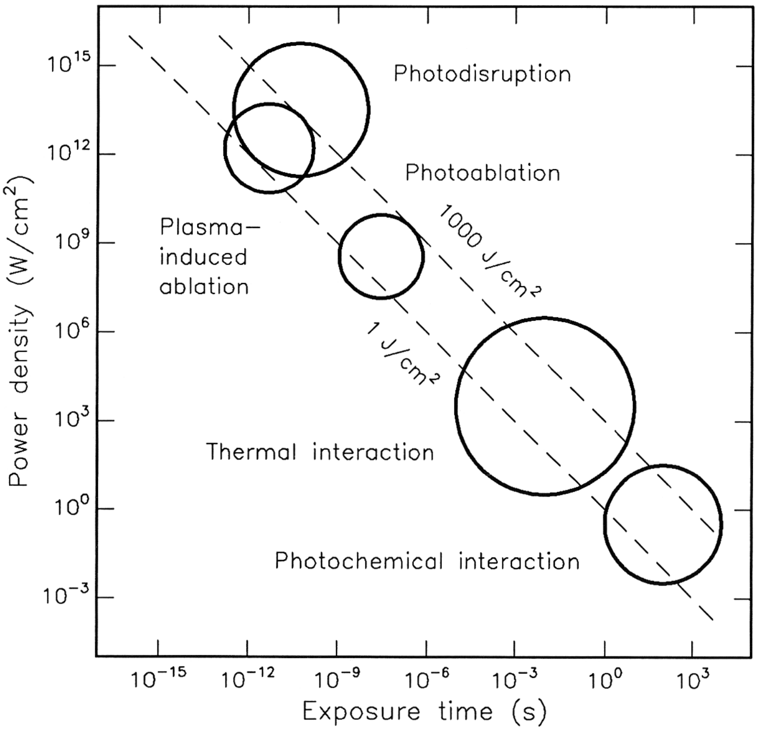

Figure 4.10: Laser-Tissue interactions [56].

durations: 1 μs to 1 min, typical power densities: 10-10^6 W/cm^2). The resulting temperatures depend on the duration and intensity of the laser light. The optimal laser (wavelength) depends on the absorption properties of the tissue. A commonly used laser for thermal interaction is the CO_2 laser emitting light at 10.6 μm. The light is absorbed at the surface of the tissue. The absorption coefficient of water depends on the wavelength of the radiation (Fig.4.11). Absorption is minimal between 700 nm and 1100 nm. Light is able to penetrate water (a main component of the cell) very deep, therefore this region is called 'therapeutic window'.

The radiation of the laser (Nd:YAG; 1.064 μm) used for coagulation in stereotactic neurosurgery penetrates the tissue up to a few mm. It is especially suitable for the required coagulation of the blood vessels in neurosurgery, because the absorption coefficient of blood is 100 times higher than that of brain tissue, i.e. blood is heated up stronger due to the higher energy deposition. This property enables the coagulation of blood vessels in the brain without causing bleedings.

It is difficult to use the right amount of energy due to the heat conduction in the tissue. The appropriate energy level has to be chosen because heat diffusion affects surrounding tissue (Fig.4.12). Exposure time, pulse length, and repetition

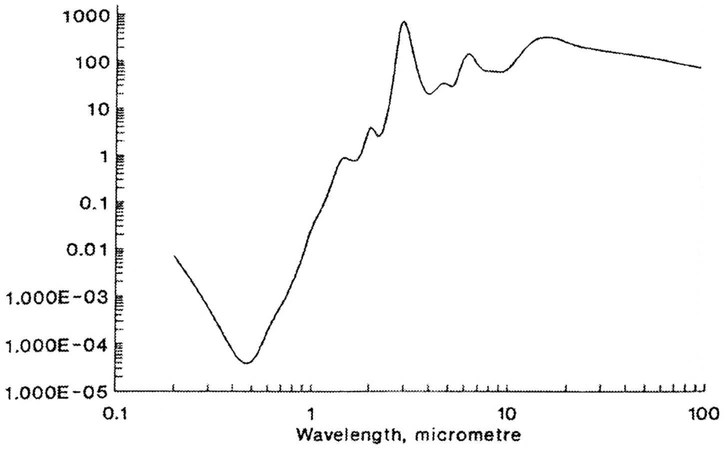

Figure 4.11: Optical attenuation coefficient (in mm^{-1}) for water [57]. For wavelengths between 700 and 1100 nm the absorption is very low, the so-called "therapeutic window".

rate of the laser have to be chosen to fit the current operation conditions, which depend on the diffusion properties, thermal conductivity, and the specific heat of the tissue. Due to the isotropic property of heat diffusion, the accurate coagulation of the tumor seems to be nearly impossible, even if the exact optical and thermal properties of the tissue are known. Thermal effects caused by irradiation are shown in Fig.4.12 and listed in Table 4.1.

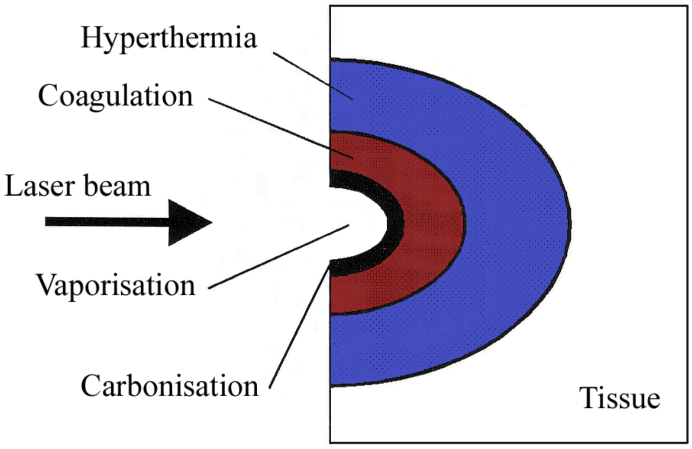

Figure 4.12: Location of thermal effects of laser radiation in tissue.

Temperature	Effect in the tissue
45° C	Hyperthermia, shrinking due to changes in the cell membranes
50° C	Lower activity of enzymes, cell immobility
62° C	Coagulation, denaturation of proteins causes coagulation
80° C	Permeabilization of membranes
100° C	Vaporization, thermal decomposition (ablation)
over 150° C	Carbonisation
over 300° C	Melting

Table 4.1: Thermal effects of laser radiation.

4.4.3 Photo ablation

Chemical bonds are broken by very high energies of the used photons (several eV) [55].

$$h\nu + \mathrm{AB} \longrightarrow \mathrm{A} + \mathrm{B}$$

Wavelengths in the UV are needed, therefore eximer-lasers are used (for example an ArF eximer laser with a wavelength of 193 nm (photon energy: 6.4 eV). The photon energy exceeds the dissociation energy of many chemical bonds ($C = C$: 6.4 eV; $O - H$: 4.8 eV; $C - C$: 3.6 eV)). These lasers are used for the ablation of corneal tissue in refractive corneal eye surgery. Typical lasers for photo ablation have pulse durations of 10-100 ns and the used power densities are in the order of 10^7-10^{10} W/cm^2.

4.4.4 Plasma-induced ablation

Optical breakdown occurs if power densities exceed 10^{11} W/cm^2 in fluids and solids or 10^{14} W/cm^2 in air. With these densities, a plasma, i.e. a high ionized state, is induced, and a plasma spark is visible. There are two possibilities to initiate the generation of a plasma: either with pulses in the nanosecond range or with pulses in the pico- and femtosecond range. With nanosecond pulses the tissue initially heats up to over 1000 K and thermal ionization takes place. With pulses in the pico- and femtosecond range, the high photon density enables coherent absorption of several photons providing enough energy for multi-photon ionization. In both cases some (so-called 'lucky') electrons absorb further energy from the radiation field by inverse bremsstrahlung. Larger amounts of atoms and molecules are ionized by these accelerated electrons, therefore initiating an avalanche effect. Within a few picoseconds, a plasma with very high electron

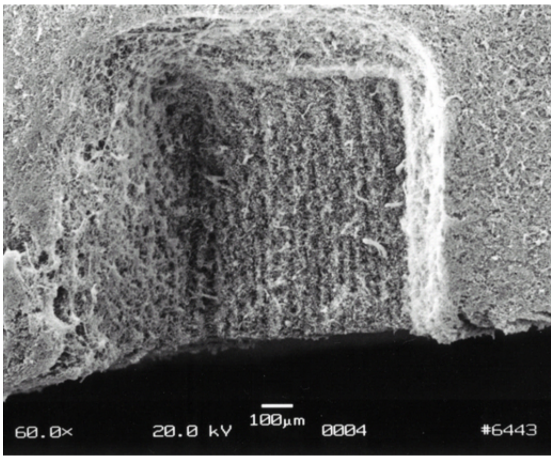

Figure 4.13: EM picture of an ablation pattern (size: 1 mm^3) in brain tissue of a pig. Ablation is done with a ps-laser. The picture shows the accuracy of ablation and the little damage to the surrounding tissue.

density (10^{21} cm^{-3}) is generated. The correlation between the minimal energy density ϱ_{th} and pulse duration t_p is the following:

$$\varrho_{th} \propto \sqrt{t_p} \tag{4.14}$$

Plasma generated in water (tissues with high water contents are effected as well) induces shock waves. These shock waves propagate with twice the velocity of sound for the first 100-200 μm, after which they propagate with the velocity of sound (1480 m/s). Upon vaporization of the liquid at the plasma, a cavity is formed. The radius of the damaged area is of the same radius as the maximum radius of cavitation bubbles, therefore implying, that the forming of cavitation bubbles is the process mainly responsible for ablation. The equations 4.14 shows, that with shorter pulse durations the energy needed for generation of a plasma and the region affected by the process decrease. For precise ablation of tissue, short pulses with energies near the threshold energy have to be chosen. With plasma induced ablation it is possible to locally resect small pieces of tissue with high precision (Fig.4.13). With the used laser system the ablated volumes have side lengths of about 50 μm.

4.5 Laser Systems

In stereotactic laser neurosurgery different laser systems are required. Some lasers used for medical applications are listed in Table 4.2. For diagnosis a continuous wave (cw) HeCd laser is used. For coagulation and ablation infrared lasers are applied. The optical quality of a laser beam is expressed by the factor M^2. This factor describes the extent of the radius(w_0)-divergence(θ) product of the beams compared to an optimal Gaussian beam. For an ideal laser we have:

$$w_0\theta = \frac{\lambda}{\pi} \tag{4.15}$$

and for a real laser:

$$w_{0M}\theta_M = M^2\frac{\lambda}{\pi} > \frac{\lambda}{\pi} \tag{4.16}$$

Laser type	Wavelength (nm)	Typical pulse duration
Argon ion	488/514	cw
HeNe	633	cw
HeCd	325/442	cw
CO_2	10600	cw or pulsed
Dye lasers	450-900	cw or pulsed
Nd:YLF	1053	$100ns$-$250\mu s$
Nd:YAG	1064	$100ns$-$250\mu s$
Nd:YLF	1053	$30ps$-$100ps$
Nd:YAG	1064	$30ps$-$100ps$
Ti:Sapphire	700-1000	$10fs$-$100ps$

Table 4.2: Some laser systems used in medical applications.

4.5.1 Laser for diagnosis

In our setup, the diagnostic laser is a HeCd laser (IK 5652R-G, Kimmon electric co., ltd, Tokyo, Japan), which delivers 100 mW at the used wavelength of 442 nm. In addition, the laser delivers 30 mW in the UV at 325 nm. The emitted wavelengths can be selected (no emission, 442 nm, 325 nm, or 442 nm and 325 nm) with a shutter/wavelength-selector at the laser aperture.

4.5.2 Lasers for ablation

As for plasma-induced laser ablation high energy pulses with short durations and high repetition rates are needed, an appropriate laser system is required [58]. Two laser systems have been used for stereotactic laser neurosurgery applications:

The Nd:YLF laser system

This Nd:YLF laser system was developed in our department. The system delivers laser pulses with a duration down to 30 *ps* and energies up to 1 *mJ* with a repetition rate of 1 *kHz*. The wavelength is 1053 *nm* and is therefore within the scope of the therapeutic window. That means the attenuation in tissue at this wavelength is rather low, allowing penetration of the tissue. This laser consists of two parts: an oscillator and a regenerative amplifier.

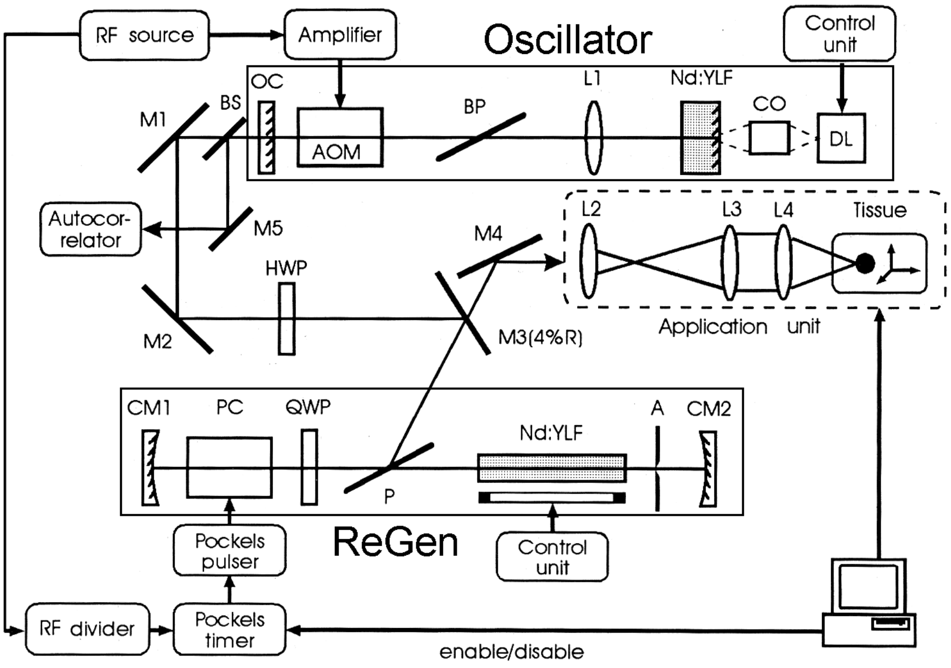

Figure 4.14: Schematic drawing of a Nd:YLF ps-laser system. OC, AOM, BP, L1, Nd:YLF, CO and DL (upper half) form the Oscillator. CM1, PC, QWP, P, Nd:YLF, A and CM2 form the ReGen.

In the oscillator and the regenerative amplifier the active medium is an Yttrium-Lithium-Fluoride-crystal dotted with 1.5 % of neodymium^{3+}-ions. Light pulses are formed in the oscillator by mode coupling with an acusto-optic modulator (AOM). These pulses of duration of some picoseconds have energies of about 0.2 *nJ*.

In the upper part of Fig.4.14 the oscillator is shown. Ultra short pulses with a low energy (30 *mW*) are generated with a repetition rate of 160 *MHz*. The backplane of the Nd:YLF crystal is one of the two resonator mirrors. The laser diode (LD) pumps the crystal longitudinally. The TEM_{00} mode is favored in this setup. The AOM generates an optical grating. An 80 MHz signal, applied to the AOM, generates a train of short pulses with durations of about 25 ps. The autocorrelation system allows the check of the pulses' width. With the brewster plate (BP) the 1053 nm transition is selected. At the half wave plate (HWP) the polarization vector (160 MHz, 0.2 nJ) of the pulse train is rotated by 90°. Mirror M3 (4% reflectivity) and the polarizing beam splitter (P) injects the pulses into the regenerative amplifier (ReGen). The ReGen is shown in the lower part of Fig.4.14. It consists of two 76 mm Nd:YLF rods, pumped by xenon lamps and a Pockels cell (PC). The cavity is formed by the two highly reflective mirrors (CM1, CM2) with a curvature of 1 m. The Pockels cell, a $LiNbO_3$ crystal, provides half wave retardation per round-trip by applying 2 kV voltage. In combination with the half wave retardation of the quarter wave plate (QWP), a selected oscillator pulse is seeded and trapped in the ReGen unit. After about 100 round trips the Pockels cell is switched to 0 kV, leading to loss of retardation. The polarization vector is rotated by 90° by twice passing the quarter wave plate (QWP). The amplified pulse is then reflected at the beam splitter (P) and dumped out of the ReGen. The pulse energy can be increased up to 1 mJ by amplification. The aperture (A) restricts the laser to the $\mathrm{TEM}_{0,0}$ mode. 96 % of the dumped pulse are reflected out of the laser system by mirror M4 and can be used for tissue experiments.

This laser system needs high power electrical supply (three phase supply with 400 V, 64 A) and water (at least 50 l per minute) for cooling of the xenon lamp pump heads. For the first experiments in the animal facility in Leuven (Belgium) [59] an extensive installation had to be done before the experiments could be conducted.

The Nd:YAG laser system

The second laser system evaluated was the HARP picosecond laser from Time-Bandwidth. This is the actually used laser for ablation in stereotactic laser neurosurgery. This laser consists of three parts: the oscillator, the regenerative amplifier, and an amplifier. All laser media are pumped by laser diodes.

The oscillator is realized by a SESAM (semiconductor saturable absorber mirror) realizing a passive mode coupling and a Nd:YVO_4 diode pumped laser. The mirror opens after saturated absorption, and a pulse of 10 nJ is emitted.

The second unit is a regenerative amplifier. Its laser medium is pumped by a 20 W laser diode. A Pockels cell switches the cavity with a repetition rate of 4 kHz from dumping to seeding. The output power of this ReGen is 1.6 W.

The third unit is not a laser, because no end mirror is implemented. This unit serves as a four pass amplifier. The active medium is a Nd:YAG crystal with a diameter of 4 mm and a length of 105 mm. The rods are pumped by pentagonal laser diode arrays with an electrical power of 1.4 kW. After four passes through the amplifier the pulses are amplified to an output power of 10 W. The laser delivers a beam with $M_x^2 = 2.1$ and $M_y^2 = 2.9$ in x- respectively y-direction.

The advantage of this setup is that for supply only regular $230V/16A$ sockets are required. The cooling is done by closed water cooling, which transmits the energy to the surrounding air. Thus, no water connection is needed.

4.5.3 Laser for coagulation

For the coagulation of blood vessels an industrial laser system was used. A lamp pumped Nd:YAG laser with a wavelength of 1.064 μm produces a typical output power in the TEM_{00} mode of 28 W. As the laser is intended for industrial use the beam quality is not optimal ($M^2 \approx 1.3$, M gives the factor to which extent the real beam is bigger than a theoretical Gaussian beam). This laser has to be cooled with a double circulation water cooling.

4.6 Beam guidance

This section describes how the laser radiation is applied to the patient. In the neurosurgery facility of the University of Cologne, the laser systems are installed in a room near the operating theatre. Therefore, a distance of 10 m has to be spanned. The distance is bridged using an optical tunnel with beam guiding optics. The use of optical fibers is not possible due to the high intensities of the laser beam. In mono-mode fibers the energy density would be far too high and the fiber would be destroyed. As an alternative, a thick optical fiber could be used, but in this case the beam quality would degrade to such an extent, that the beam could just be focused down to a size of the optical fiber [60]. Its focal spot size would not be sufficiently small to get plasma-induced ablation in the tissue. The laser beam is guided to the laser probe by an articulated mirror arm.

If different beam diameters are required, a telescope has to be used. The best choice for this application is to use a focus-free Galilei telescope in order to avoid the generation of plasma sparks inside the telescope. The articulated mirror arm has to be adjusted very precisely, otherwise no radiation can pass the arm. For the online-correction of the deviations due to movements of the arm, an automated beam-adjustment is integrated into the arm [61]. The position of the beam is detected by four-quadrant diodes and, if necessary, readjusted by motor-adjustable mirrors.

4.7 Software engineering

For the control of the setup and display of the data, a C++ program was developed using the QT-libraries [62, 63]. A detailed description of the program is given in chapter 5.3.

Chapter 5

OligoChannel Spectrum Analysis

As described in chapters 2 and 3, the OligoChannel Spectrum Analyzer (OCSA) was developed in order to overcome the disadvantages of the OMA, because high signals and long exposure times are not available in neurosurgery [64]. Therefore, a combination of the two types (point spectroscopy, analyzing the spectrum of one point in the sample [48] and fluorescence imaging [47]) of fluorescence detectors has been developed: the OCSA [65, 66]. The aim is to do fast (up to MHz-range) and sensitive analysis. We try to keep the advantages (sensitivity, speed, and significance) of both systems, while overcoming their disadvantages.

5.1 Analysis

Results in literature [27] and results of our own experiments [28] show, that there is enough information in the autofluorescence spectra of the different types of tissue for reliable distinction between them. The only problem is to access this information. The following access is widely used:

For a certain application (e.g. the distinction between healthy and cancerous lung tissue) spectra of the different tissue types are obtained.

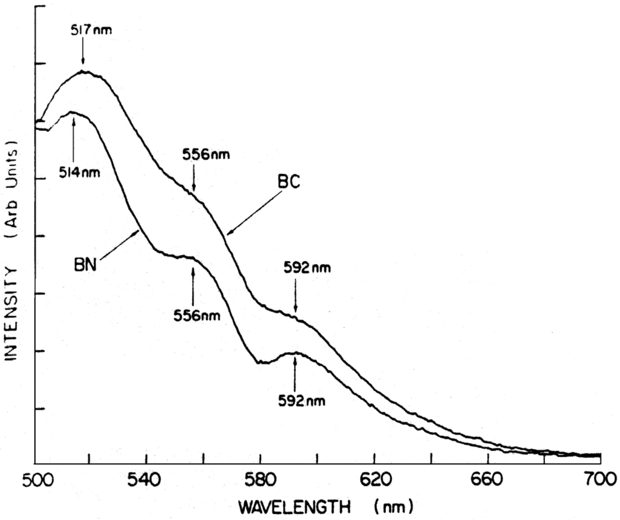

Figure 5.1: Spectra of normal (BN) and cancerous (BC) human breast tissue. The tissue is illuminated with an excitation wavelength of 488 nm (Argon laser) and the emitted spectrum is recorded by an OMA. The main maximum is shifted and the side maxima are reduced in cancerous tissue.

As an example, the autofluorescence spectra of normal (BN) and tumor (BC) human breast tissues are shown in Fig.5.1 [27]. The endogenous fluorophores in the tissue are photoexcited at 488 *nm* and observed from 500 *nm* to 700 *nm*. The main spectral peaks are located at 514 *nm* for normal and at 517 *nm* for tumor tissue. In addition, there are two subsidiary peaks at 556 *nm* and 592 *nm* in healthy tissue, whereas the spectrum of tumor tissue shows a monotonic decrease with no clear side maxima. In the observed sample the location of the main maxima varies at different points in the sample from 514 *nm* to 516 *nm* for normal tissue and from 517 *nm* to 519 *nm* for tumor tissue. Fluorescence studies have shown that the spectral maxima of proteins which contain fluorophores are shifted to higher wavelengths after gaining negatively charged ions [67]. Therefore, analysis of the location of the main maxima can provide information about the type of tissue. Another possibility to access information inside autofluorescence spectra is to examine the side maxima: The tissue is healthy if side peaks can be found. A method described in literature is the division of the intensities at 556 *nm* and 592 *nm* by the intensities at 550 *nm* and 580 *nm*. This gives values of 0.91 and 0.94 for cancer tissue and 1.0 and 1.1 for healthy breast tissue. Therefore, all tissue samples with these values smaller than 1 can be considered to be cancer tissue.

Since the differences between the spectra have to be found individually for every specific application, a more general approach had to be found. Another approach for the development of a new method was the fact that optical multichannel spectra (about 600 channels) cannot be obtained with the required quality in the required time due to low light intensities in each channel. The solution to this problem is a system with a reduced number of detectors. This has two main advantages: First, we do not have to spread the small amount of available photons over hundreds of detectors, which gives us better detection statistics. Second, discrete high-sensitive devices (like photomultiplier tubes) instead of CCD devices, which have lower sensitivity/quantum efficiencies can be used.

The goal was to classify the tissues with a reduced number of channels in the detection system. For a working model the following assumptions were made:

- The system contains just a given number of reference tissues. Every observed point can be presented as a combination of these reference tissues.

- For mathematical simplicity, the same number of references and detectors is used. Otherwise the system of equations would be under- or overdetermined.

- The reference tissues have distinguishable spectral patterns. The reference vectors are independent.

In the analytic model for analysis described here, it is assumed that there are only three types of tissue at any area of interest. Thus, each observed focal point $\vec{e}$ can be described as a combination of these three references:

$$\vec{e} = x_1\vec{a} + x_2\vec{b} + x_3\vec{c} \tag{5.1}$$

or

$$\vec{e} = \mathbf{A}\vec{x}. \tag{5.2}$$

The results described below were collected with a system of three detectors. Therefore the analysis will be explained for the 3-dimensional case, i.e. there are three detectors and three different reference tissues. For each point in the specimen three values are obtained, representing a vector in the space of possible sets of values. Each value represents the autofluorescence intensity in a certain range of the spectrum at the observed point of the specimen. For an analytic device in stereotactic laser neurosurgery, a larger number of detectors (dimensions) should be taken into account, which would increase the complexity of the system.

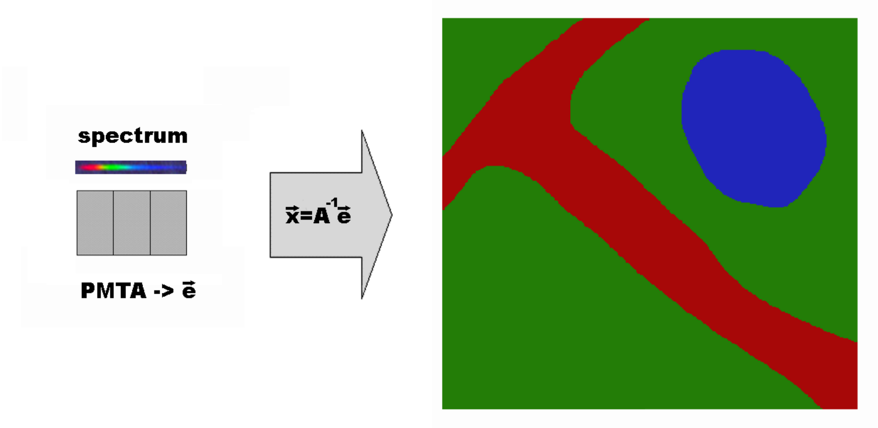

Figure 5.2: The analysis (OCSA-Transformation) of the spectra leads to a functional picture.

In the first step, the device needs to be calibrated with three tissue samples (references). The vectors $\vec{a}$, $\vec{b}$, $\vec{c}$, representing the spectral intensities in the three detection wavelength bands, are recorded and transferred to a 3x3 matrix **A**. The matrix contains the three spectral 'fingerprints' of the three references (tissue samples):

$$\vec{a}, \vec{b}, \vec{c} \Rightarrow \mathbf{A} = \begin{pmatrix} a_1 & b_1 & c_1 \\ a_2 & b_2 & c_2 \\ a_3 & b_3 & c_3 \end{pmatrix}. \tag{5.3}$$

Calibration has to be done carefully, since the more exact the spectral fingerprints of the reference tissues are taken, the more precise the classification of the observed tissue will be. Usually an averaged spectral fingerprint of a certain area of the reference sample is taken. During the surgical process it is necessary to know which fractions (x_1, x_2, x_3) of the three reference tissue types are present in the observed volume of the tissue sample. As there is no relevant information in the absolute intensity of the signal, all obtained vectors are 'normalized': Each value of the vector is divided by the sum of the three values of the vector.

The intensity of the signal is mainly influenced by the light-transmittance of the material between the observed point and the optics or by slight out-of-focus influences. Therefore, this information is not used for the given problem. In contrast, the relative intensities of the wavelength bands are mainly influenced by the biochemistry of the cell and are therefore dependent on the type and the status of the observed tissue. Vector $\vec{x}$ contains the entire information about the composition of the sample volume. To obtain this vector, the inverse matrix of $\mathbf{A}$ is used. This inversion has to be done just once at the end of the calibration process. During the rest of the measurement the three values received from the PMTs have to be multiplied with the inverse matrix $\mathbf{A}^{-1}$ (OCSA-Transformation):

$$\vec{x} = \mathbf{A}^{-1}\vec{e}. \tag{5.4}$$

Vector $\vec{x}$ represents the fraction of reference tissues in the sample volume. If $\vec{x}$ can be clearly associated with one type of tissue, the pixel in the image is color coded, corresponding to the type of tissue (Fig.5.2). A functional picture is obtained. This information is submitted to the surgical system, which decides what do do with the sample volume (coagulation, ablation, no action).

5.2 Experimental setup

In stereotactic neurosurgery tissue samples are observed by a conventional confocal laser scanning microscope, which is integrated in the probe [37]. A confocal setup has to be used in order to suppress signals from beyond the observed point of tissue (chapter 4.3). The OCSA serves as a point detector in the confocal microscope.

For our experiments a tabletop setup is used (Fig.5.3). The laser is a HeCd laser (IK 5652R-G, Kimmon electric co., ltd, Tokyo, Japan), which delivers 100 mW at the used wavelength of 442 nm. The beam splitter BS1 (344132: 20x30 mm^2, BK7, R=10 %, T=90 %, Linos Photonics GmbH, Göttingen, Germany) is used to lower intensity; it divides the beam into two parts. The reflected

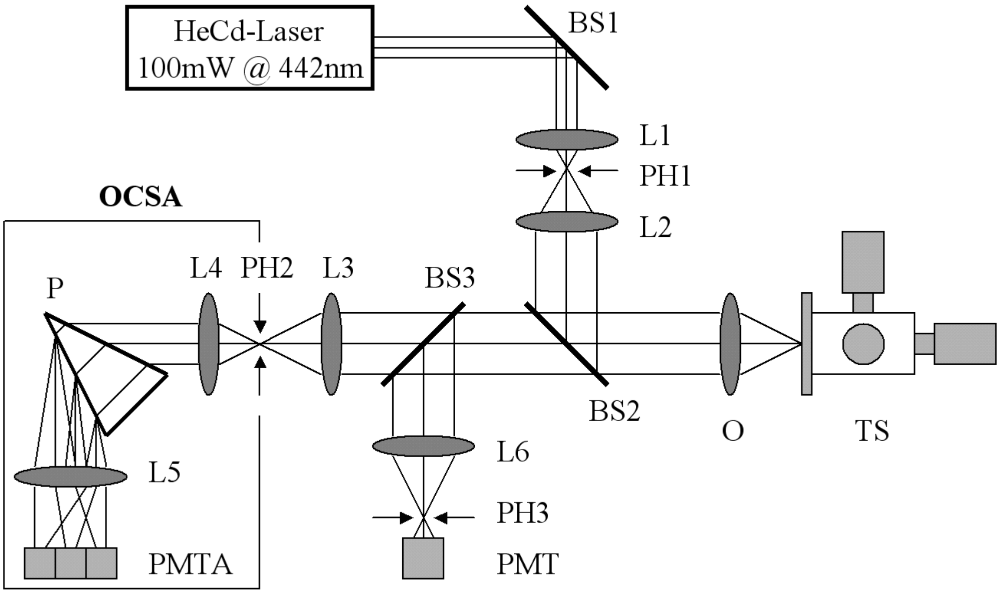

Figure 5.3: Experimental setup with OligoChannel Spectrum Analyzer (OCSA) for tissue detection: A HeCd-Laser is used as a light source. The first beam splitter (BS1, reflectivity: 10%, transmission: 90%) reduces the intensity of the emitted beam, lens 1 (L1), pinhole 1 (PH1) and lens 2 (L2) serve as a beam expander and a spatial filter to maintain high beam quality. This part of the setup is the point source in the confocal setup. Beam splitter 2 (BS2, reflectivity: 10%, transmission: 90%) reflects 10% of the light onto the objective lens (O), which focuses the light onto the sample on the translation stage (TS). 90% of the light emitted by the probe and collected by the objective lens are transmitted through beam splitter 2 (BS2) onto the detection system. The dicroic beam splitter (BS3) separates the light into the excitation wavelength and the rest of the spectrum. The excitation wavelength is reflected onto a point detector consisting of of L6 (focusing lens), PH3 pinhole, and a photomultiplier tube (PMT). The transmitted spectrum is analyzed in the OCSA, which is also a point detector: The light is focused onto the pinhole 2 (PH2). Therefore the OCSA serves as a point detector in the confocal setup. Lens 4 (L4) forms a parallel beam, prism (P) refracts the light dependent on the wavelength into different directions. Lens 5 (L5) refocuses the light onto a detector array (PMTA). A spectrum with only a few channels is collected.

10 % (real: 17 mW) are used for our experiments, 90 % of the intensity are transmitted and rejected. The rejected part of the beam could be used for other experiments (see discussion). The beam is expanded to a diameter of 8 mm by

two standard microscope lenses L1 (04 OAS 016: 40x0.65, Melles Griot, Irvine, USA), L2 (04 OAS 006: 4x0.12, Melles Griot, Irvine, USA) and a pinhole (diameter 20 μm). Behind the beam expander the intensity has dropped to 4 mW. The actual beam splitter for the confocal setup is beam splitter BS2 (344132: 20x30 mm^2, BK7, R=10 %, T=90 %, Linos Photonics GmbH, Göttingen, Germany). The use of this beam splitter has the advantage, that most (90 %) of the light emitted by the probe in the acceptance angle of the objective O (04 OAS 010: 10x0.25, Melles Griot, Irvine, USA) is transmitted to the detection unit. A light intensity of 10 % (0.65 mW on the sample) was shown to be sufficient for this setup in our experiments. As we wanted to examine tissue *in vivo*, the exposure should be kept as low as possible. The translation stage (TS) consists of a x-y-z stage for rough positioning of the probe and, mounted onto this, a piezoelectric stage (PXY 400, Piezosysteme Jena GmbH, Jena, Germany; control electronics: MRC-Systems GmbH, Heidelberg, Germany) for x-y scanning with a range of 400 μm. In the laboratory experiments, object scanning instead of beam scanning was is for simplicity. The tissue sample is mounted onto the piezoelectric actuator and fixed between two cover slips. The dicroic beam splitter BS3 (glass plate with custom coating dlhs 308, Melles Griot, Irvine, USA) divides the light, which is emitted by the sample volume into the excitation wavelength of the laser and the rest of the spectrum. The transmitted part of the spectrum is analyzed by the OCSA: The light is focused by L3 (04 OAS 010: 10x0.25, Melles Griot, Irvine, USA) through the pinhole PH2 (diameter 25 μm), thus the OCSA (Fig.5.3:OCSA) can be considered as a point detector in the confocal setup. A picture of the laboratory setup is shown in Fig.5.4. The light crossing the pinhole PH2 is formed into a parallel beam by lens L4 (04 OAS 006: 4x0.12, Melles Griot, Irvine, USA). The prism P (336672, SF10, 30 mm x 30 mm, Linos Photonics GmbH, Göttingen, Germany) deflects the light into different directions (dispersion) dependent on the wavelength; Lens L5 (063215, f=120 mm, Linos Photonics GmbH, Göttingen, Germany) refocuses the beam onto a detector array PMTA (three H 5784, Hamamatsu Photonics K.K., Shizuoka-ken, Japan). The three detectors cover the spectral ranges as follows: detector one 450-500 nm, detector two 500-550 nm, detector three 550-600 nm. The complete OCSA-setup is mounted in a light-tight box system (Fig.5.6) with light-tight electrical connection board (Fig.5.7).

A limited number of photomultiplier tubes (PMTs) is used for detection due to their high sensitivity and speed. These photosensor modules contain a built-in amplifier which limits the bandwidth to 20 kHz. The control and supply electronics was built by the electronics workshop of the Kirchhoff Institute of Physics Heidelberg. It fulfils the 4 kHz requirement of the stereotactic laser neurosurgery application. By using several detectors, much more information is obtained from the specimen compared to just looking at the overall intensity. The values delivered by the detector array ware digitized by a Data AcQuisition (DAQ) card (PCI-MIO-16E-1, National Instruments, Austin, USA) in a personal computer and analyzed as described in section 5.1.

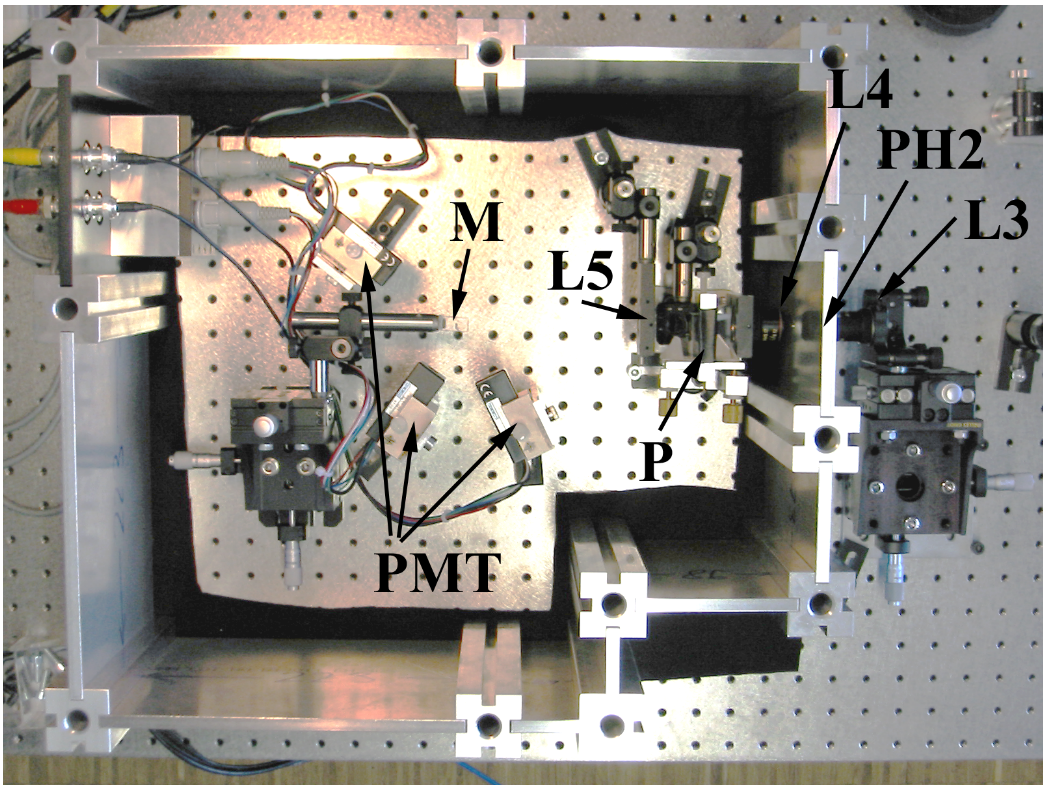

Figure 5.4: Overview of the OCSA. The light to be analyzed is focused by lens (L3) onto the pinhole (PH2). The light enters the light-tight box (Fig.5.6) through the pinhole and is collimated by lens (L4). The prism (P) spreads the light, which is refocused by a lens (L5) onto the micro-mirror (M). The micro-mirror distributes the light over the detectors (PMT). The micro-mirror and the PMTs form the detector array (Fig.5.3:PMTA).

As we wanted to use discrete photo multiplier tubes (PMTs), the light had to be distributed among the PMTs. The actual hole for incoming light in the housing of a PMT is quite small compared to the size of the whole sheath. Thus, by spreading the spectrum over this array, part of the light would hit the housing and not the light sensitive opening window, if the tubes were arranged close to each other. Since in our experiments no waste of light can be accepted due to the fact that very low light levels are available, the following setup was used:

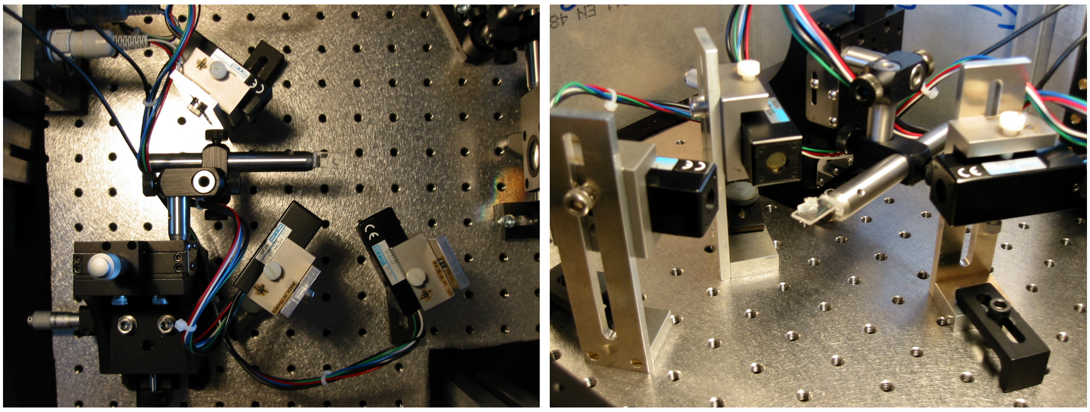

Figure 5.5: Detailed views of the micro-mirror PMT setup.

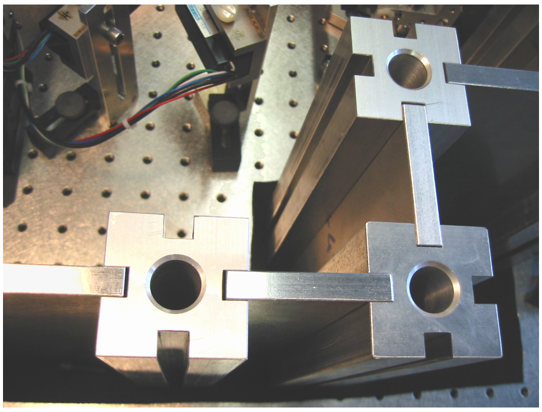

Figure 5.6: The light-tight housing for the OCSA consists of elements for the edges and pieces for the wall inserted between two of the edge elements.

The light entering the detection unit through the detection pinhole (PH2) is collimated by a lens (L4) into a parallel beam. This parallel beam is crossing a prism (P). Dependent on the wavelength of the photons, an angular dispersion is added to the wavelength. This beam with the imprinted wavelength-dependent dispersion is refocused by a lens (L5). The lens does not refocus the beam to a focus spot, because the color dispersion of the prism results in expansion of the focal spot to a focal line. The wavelength with angular divergence is refocused off the optical axis of the lens. In this focal line, a micro-mirror (M) with four facets is installed. Dependent on the wavelength the light is reflected into four different directions. No light is wasted, because the filling-factor of the micro-mirror is close 100 %.

As there was no suitable commercial mirror available and the glass workshop of the university was not able to cut such mirrors without destroying the reflective

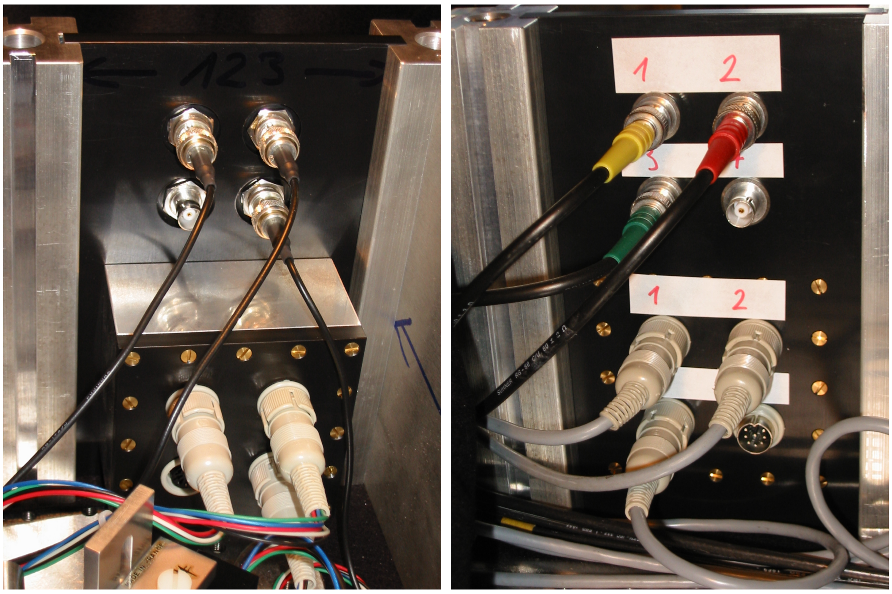

Figure 5.7: The electrical signals have to be conducted by a light-tight connection board integrated into the light-tight housing for the OCSA. left: inner view; right: outer view.

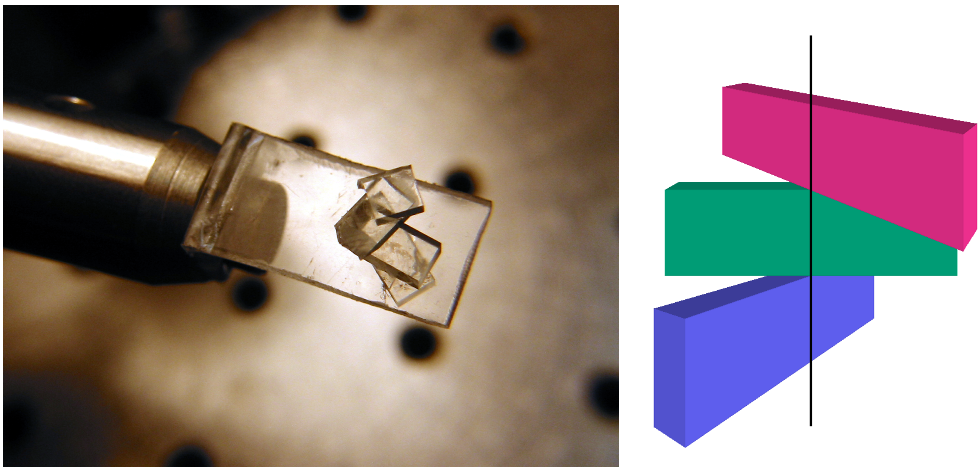

Figure 5.8: left: Close up of the micro-mirror (four facet version) array built for the experiments. right: Schematic drawing of the micro-mirror; the reflecting surfaces (planes) of the mirror facets intersect in a line (black line).

surface, A device had to build in order to cut the mirrors. The device consists of a rapidly rotating miniature cutting disk and a translation table. The translation table is driven by a stepping motor, enabling a precise an extremely slow movement (5 *mm* per hour) of the glass. The piece of mirror is clamped in a small vice on the translation stage. Small stripes, 1 *mm* to 2 *mm* in height and about

7 *mm* in length were cut from a mirror. Due to the slow feed, the surface of the reflective mirror remains unaffected. Four of these small mirror parts are glued together in such a manner that the four planes of the mirrors intersect in one line (Fig.5.8). The light divided by the prism is refocused exactly onto this line. The height of the mirror elements lays down the size of the wavelength band picked by one mirror element. In the experiments described, mirror elements with a height of 1.9 *mm* were chosen. With the used prism and the 120 *mm* refocusing lens this results in wavelength bands of 50 *nm* (see chapter 4.1). In our experiments the device was calibrated in order to pick three bands (450-500 *nm*, 500-550 *nm*, 550-600 *nm*).

5.3 Software implementation

The whole system is controlled by a C++ program [62, 63]. A graphical user interface (GUI) based on the QT library eases the application of the OCSA system. The QT environment offers a palette of components required to create a user interface, like buttons, sub-windows, frames, sliders, text windows, etc. Platform-independent and object-oriented design assures easy expansion and integration into the stereotactic neurosurgical environment used for planning and control. With in the QT toolkit a 'signal-slot concept' is available for handling of actions triggered by other actions, like pressing a button. Any part of the program can send a signal. The signal is received by an other part of the program to read out a status and start an action. In the OCSA program, the signal-slot concept is used for all the buttons on the graphical user interface.

In the main application window different functions are available.

- Single: A single image is obtained with high quality (mean of 1000 measurements).
- Continuous: This starts a continuous imaging process.
- FastScan: An image is taken with high speed.
- Stop: The actual measurement is stopped.
- Config: This button opens the configuration window, which is used for calibration of the system.

The 'Single'-scan button starts the acquisition of a single image of high quality. Every point of the sample is measured 1000 times in order to minimize the impairment due to statistical fluctuations in the data. This mode is generally used

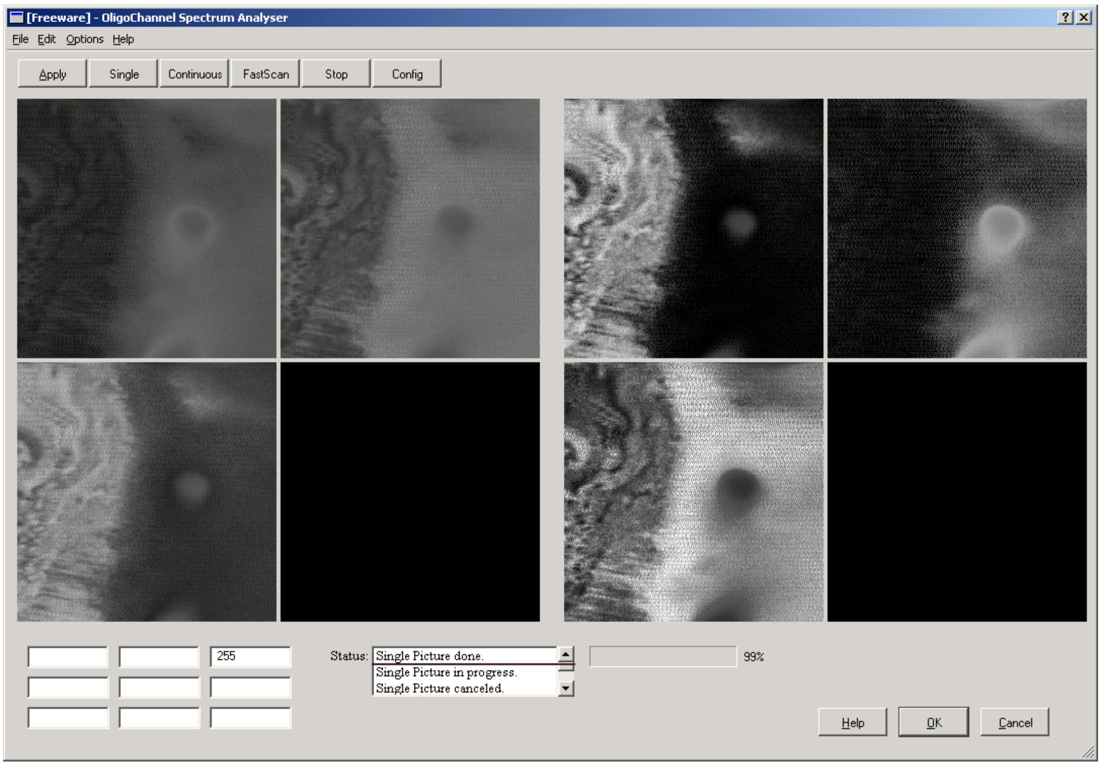

255

Status: Single Picture done.
Single Picture in progress.
Single Picture canceled.

99%

Figure 5.9: Screen shot of the graphical user interface of the implemented program.

for demonstrations, i.e. for obtaining single images of high visual quality. As one has to deal with relatively low light intensities, nicer images can be obtained in this way. As a second effect, this mode slows down the piezoelectric x-y-scanner, which leads to a better image quality, because image distortions due to limitations of the piezoelectric translation stage are reduced. Recording of a 256 by 256 pixel image takes about 10 minutes in this mode. In the real neurosurgery setup, beam scanning is used. This means that the beam is moved relative to the probe. In the used setup, the sample is moved relative to a spatially fixed beam. While scanning the sample, acceleration has to be small, otherwise the sample (biological material has no rigid structure) would move relative to the translation stage. However, much faster scanning (e.g. with beam scanning) with at least the required 4 kHz point frequency is theoretically possible.

The 'Continuous' and 'FastScan' buttons are used for measurement. The 'Continuous' scanning mode is used to look for a proper section on the sample. It is also applied to adjust the sensitivity of the PMTs. This sensitivity adjustment can be automated in future implementations, but the actual power supply and control electronics do not provide an external input for the control voltage. The high voltage (kV) of the PMTs is controlled by a control voltage (0-1 V). In future setup, this voltage may be supplied by an output card in the computer, enabling an automated determination of the best working point for a given light level.

With the 'Stop' Button the present action is terminated.

On the screen, there are two fields displaying four images each. The left four images are reserved for the intensity images obtained by the detectors. No image processing is used at this point. The vector, which is calculated from the values measured by the detectors is divided by the sum of these three values of the vector. The right four images display the analyzed data. Each channel represents the contribution of the corresponding reference tissues in the sample. Since all examples show a three-detector system, the fourth images are empty (Fig.5.9).

Pushing the 'Config' button opens a new window. The ConfigDialog window contains the tools required for calibration of the system (Fig.5.10). When the 'Reference' buttons (1-3) are pushed, a reference measurement is performed. The values are written into a matrix. The inverse matrix is calculated when the 'Inverse Matrix' button is pressed. This matrix is used in the main window for analysis.

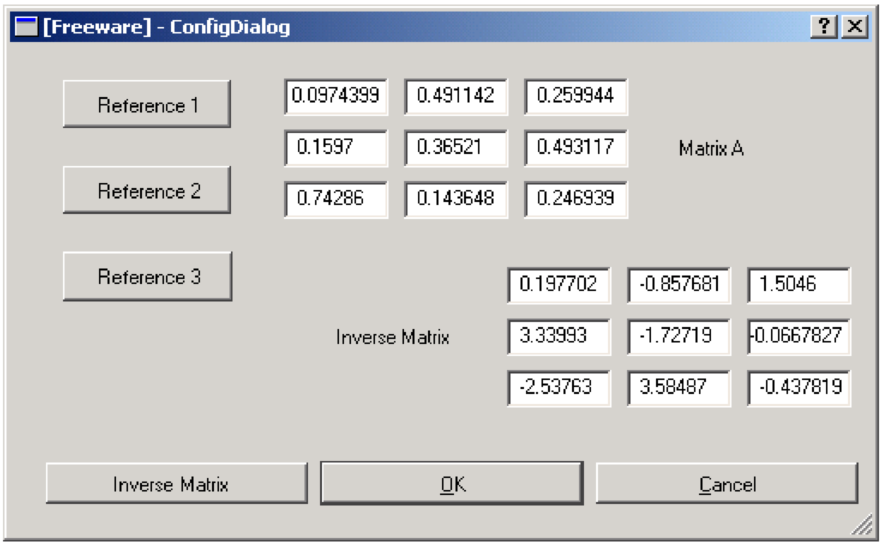

Matrix A

0.0974399	0.491142	0.259944
0.1597	0.36521	0.493117
0.74286	0.143648	0.246939

Inverse Matrix

0.197702	-0.857681	1.5046
3.33993	-1.72719	-0.0667827
-2.53763	3.58487	-0.437819

Figure 5.10: Screen shot of the configuration window for system calibration.

At the bottom of the main window of the 'OligoChannel Spectrum Analyzer' program there are several status displays (Fig.5.9). An array of nine text fields displays information about the actual scan line and the actual values (measured and OCSA-calculated) of the measured point. In addition, there is a multi-line status field to display the actual status of the system (single picture in progress, single picture done, single picture cancelled, etc.). A bar graph shows the actual progress of action.

Chapter 6

Results

6.1 Preparation of the tissue samples

6.1.1 Mouse tissue

In order to get as close as possible to *in vivo* conditions fresh tissue samples were used.

The goal in the preparation of the sample was to keep as much of the original *in vivo*-properties of the tissue observed *in vitro*. Therefore no conservation techniques were applied. Even no cooling was used in order to avoid changes in the properties of the tissue. Due to the relatively long measurement duration, only the first experiments with a set of tissue samples were really close to *in vivo* conditions.

Figure 6.1: The mouse tissue samples.

The first experiments were done with mouse tissue received from the experimental animal lab of the German Cancer Research Center (DKFZ, Heidelberg, Germany). The mouse was killed and the tissue samples were extracted immediately. Brain, heart, lung, kidney, and liver tissue were obtained (Fig.6.1).

The samples were prepared for the experimental setup in about ten minutes. No conservation techniques were used in order to maintain as many *in vivo*-properties of the tissue as possible. For each specific experiment, pieces of three of the tissue samples were arranged inside a small chamber between two cover slips in a custom made mount (Fig.6.2).

Each piece of tissue was of the size of about 5 mm^3. The mount was then fit to the piezoelectric translation stage (Fig.6.3). The experiments itself took about half an hour each, i.e. measurements were conducted over a period of 30 min.

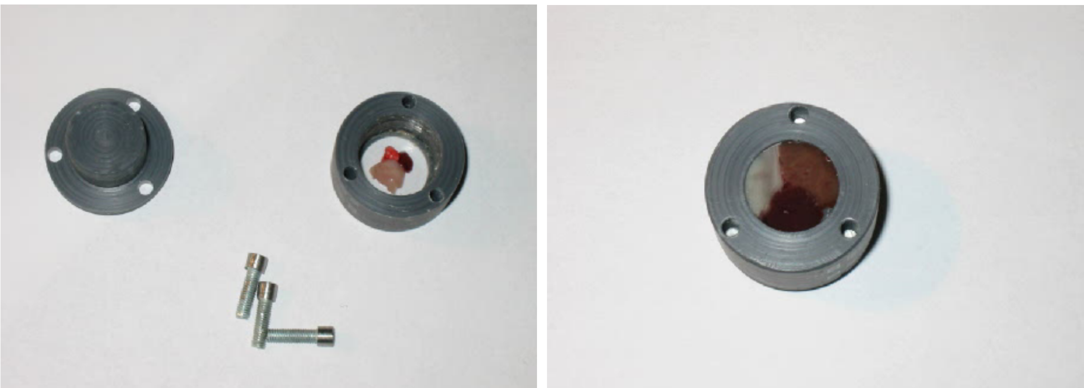

Figure 6.2: The sample mount. left: open mount with tissue samples; right: front view of the assembled mount.

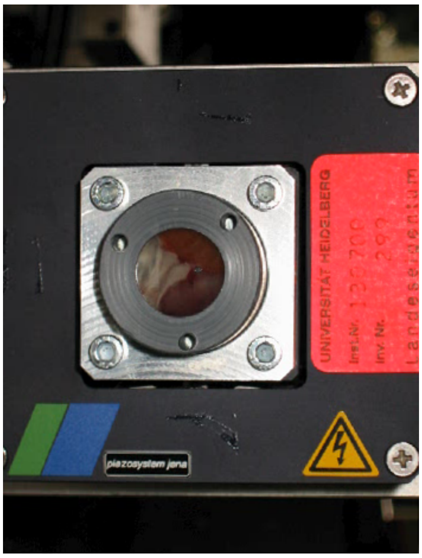

Figure 6.3: The tissue chamber mounted to the translation stage/piezoelectric scanner.

6.1.2 Human tissue

The human tissue samples were obtained from the pathology department of the German Cancer Research Center (DKFZ, Heidelberg, Germany). The specimen had been taken from a 53 year old woman, who had undergone resection of cancerous kidney tissue. In addition to the cancerous tissue a small piece of healthy tissue was obtained for comparison. This piece of healthy tissue contained a very small inclusion of fat tissue, which was used as the third tissue type for the experiments. The human tissue was processed in the same way as the mouse tissue.

6.2 Experimental results

Preliminary tests with the OCSA setup were conducted with pig tissue obtained from a local butcher's shop. All shown images have a size of 400 μm by 400 μm.

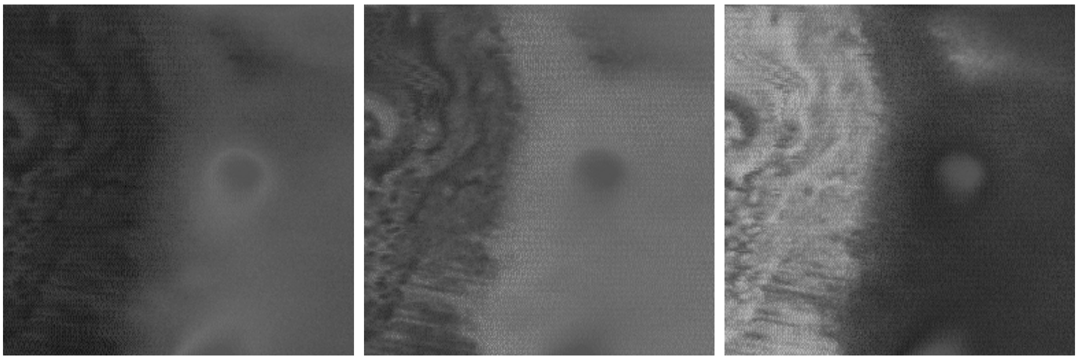

Figure 6.4: Autofluorescence signal of tissue samples obtained from the local butcher's shop. Measurements with the three photomultiplier tubes, of which signals are shown separately (left: 450-500 nm; center: 500-550 nm; right: 550-600 nm). The excitation wavelength is 442 nm.

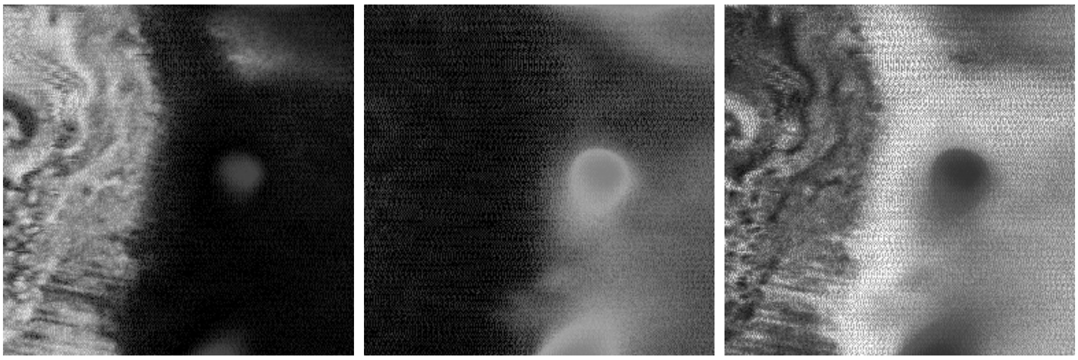

Figure 6.5: Images in the domain of the reference tissues after analysis with the OCSA-Transformation. Channel one (left) corresponds to fat tissue, channel two (center) to liver tissue and the third channel (right) represents muscle tissue.

The images in Fig.6.4 show the measured intensities, collected by the three PMTs. Fig.6.5 shows the area after analysis (in real time) with the OCSA. All three channels, corresponding to the three reference tissues, show a signal, since the intersection of all three tissues was imaged. Fig.6.6 shows a composed image of Fig.6.5. Each color corresponds to one of the reference tissues. Red corresponds to fat tissue, green to liver tissue and blue to muscle tissue. As

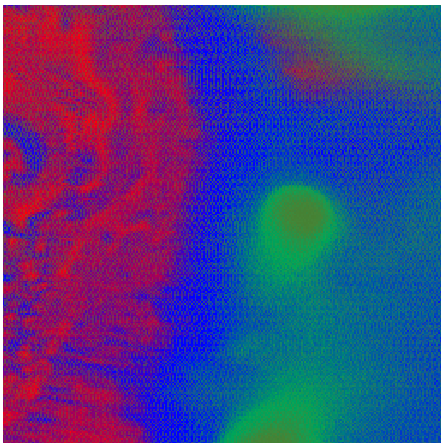

Figure 6.6: The images of Fig.6.5 are composed to a color coded image. Red corresponds to fat tissue, green to liver tissue and blue to muscle tissue.

these tests showed very promising results, further experiments closer to *in vivo* conditions were conducted.

6.2.1 Mouse tissue

The following experiments were done with a set of mouse tissues (brain, heart, kidney, liver, lung). For each experiment three of these tissues were combined on a coverslip as described in chapter 6.1. The system was calibrated as described above and subsequently transitions between two of the three tissues were imaged.

Fig.6.7 nicely illustrates the conducted experiments. Three of the mouse tissues were combined in one sample. Their geometry is shown in Fig.6.7(upper left). Three detailed images at three different transitions between the tissues were made (Fig.6.7: M1, M2, M3). This example shows that a distinction between three tissues is possible with the used setup.

The following results presented were conducted with white brain matter, grey brain matter and liver tissue, in order to demonstrate that the method works in brain applications as well.

Fig.6.8 and 6.9 show the transition from grey to white brain matter. Fig.6.8 shows the measured signals from the PMTs, whereas Fig.6.9 shows the images after analysis of the data with the OCSA (achieved in real time). The three channels are shown separately. Channel one corresponds to white brain matter, channel two to grey brain matter and the third channel to liver. After analysis with the OCSA clear signals were obtained from channel one and two, whereas channel three, which corresponds to reference tissue liver (not contained in the displayed part of the specimen) showed nearly no signal. Thus, the specificity of

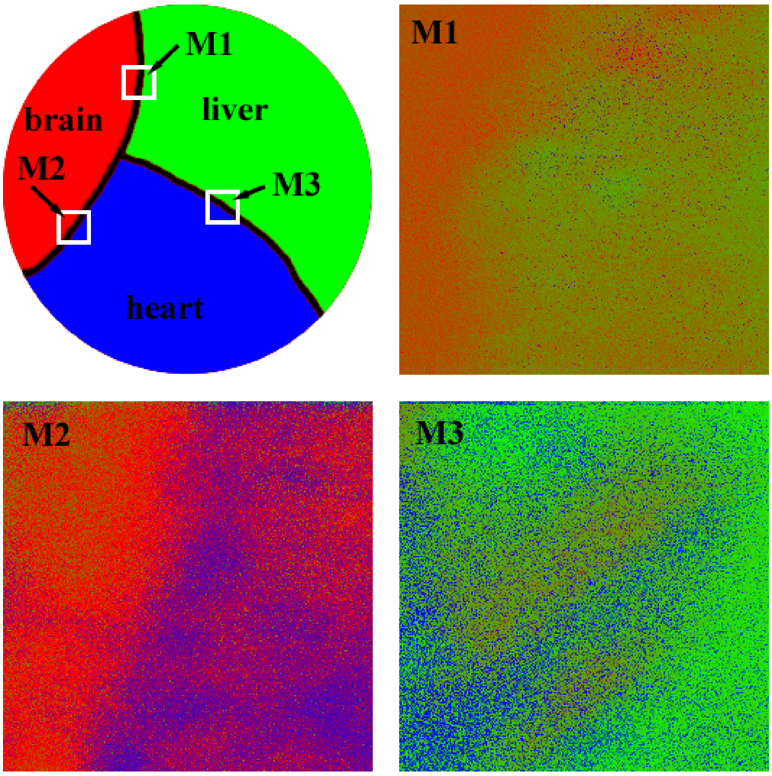

Figure 6.7: Upper left: schematic drawing of the arrangement of the tissues in the mount. M1, M2, M3: detailed images obtained with the OCSA.

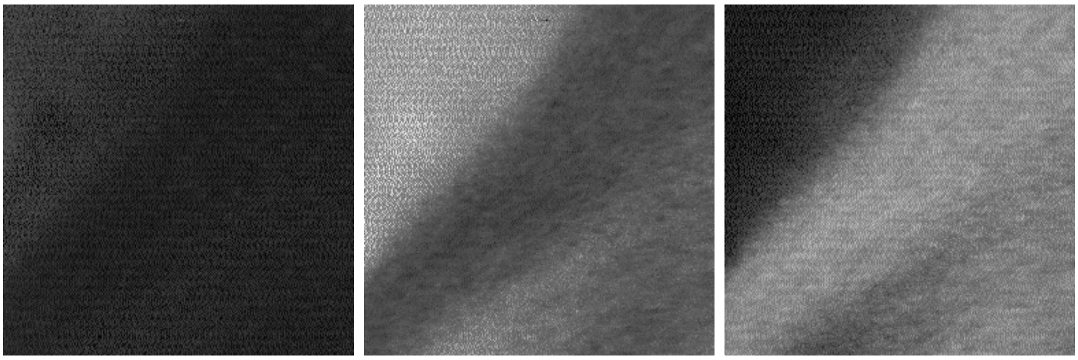

Figure 6.8: Autofluorescence signal of mouse tissue (white and grey brain matter) measured by the three photomultiplier tubes which are shown separately (left: 450-500 *nm*; center: 500-550 *nm*; right: 550-600 *nm*). The excitation wavelength is 442 *nm*. Very low contrast is visible when no image enhancements are applied.

the method was nicely illustrated. In Fig.6.10 the three channels were combined to a single color-coded image. Red corresponds to white brain matter, green to grey brain matter and blue corresponds to liver tissue.

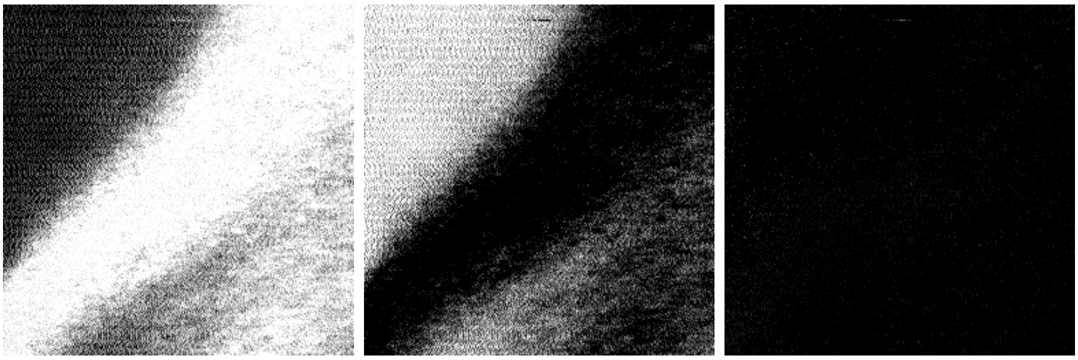

Figure 6.9: Images in the domain of the reference tissues (Fig.6.8 after analysis with the OCSA). Channel one (left) corresponds to white, channel two (center) to grey brain matter. The third channel (right) represents liver tissue, which is not present in the imaged part of the sample and therefore shows nearly no signal.

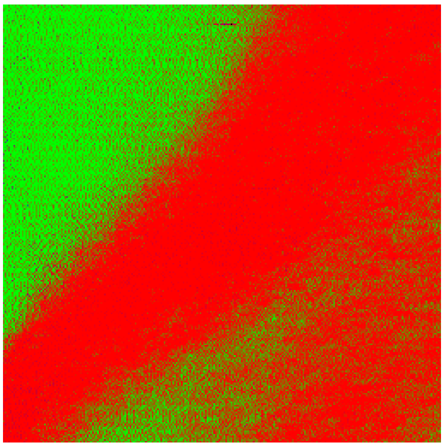

Figure 6.10: Combined image in the domain of the reference tissues. The channels shown in Fig.6.9 are combined to a color image. Red corresponds to white brain matter, green to grey brain matter and the blue color corresponds to liver tissue (not existent in the imaged region of the smple).

Each tissue sample in these triplets (any given combination of three of the mouse tissues) could be clearly determined after the calibration of the system. In Fig.6.11(left), the histogram of channel two (Fig.6.9(center)) is displayed. This histogram clearly shows that most of the pixels are zero (corresponding to white brain matter) or 256 (corresponding to grey brain matter). No special optimization is done at this point, despite the 'normalization' mentioned above (in 5.1).

Fig.6.11(right) shows the intensity of channel two after analysis with OCSA

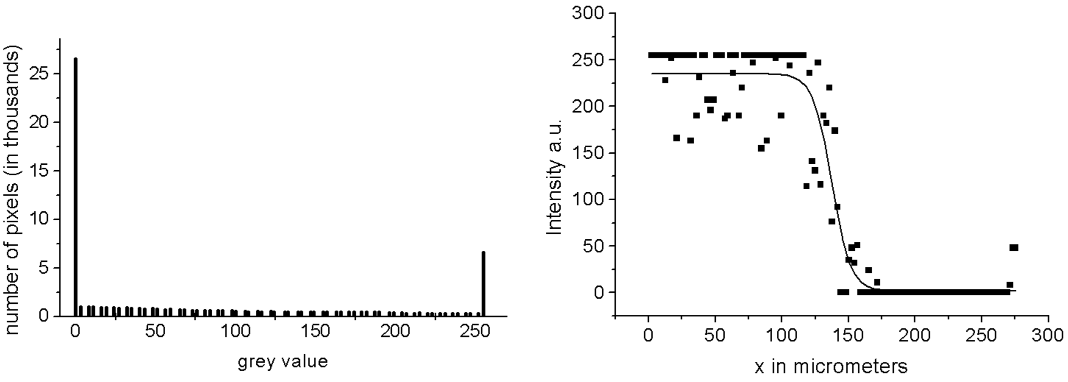

Figure 6.11: Transition from grey to white brain matter. left: histogram of Fig.6.9(center). Most of the pixels are associated with zero (in this case corresponding to white brain matter) or 256 (corresponding to grey brain matter); right: the transition is fitted with a sigmoidal curve. The intensity at the transition from grey to white brain matter falls from 90 % to 10 % along about 25 μm, indicating that the transition is detected with an accuracy of 25 μm.

along a line crossing the transition perpendicular to the borderline between grey and white brain matter. The sigmoidal curve fit to the data can be used to obtain the spatial resolution of the fluorescence microscope. The intensity at the transition from grey to white brain matter falls from 90 % to 10 % across about 25 μm, indicating that detection accuracy of a transition is 25 μm.

6.2.2 Human kidney tissue

After this successful approach with mouse tissues, further experiments were done using human tissue from a 53 year old woman, who had undergone resection of a carcinoma in the kidney. Three types of tissue were used: kidney carcinoma, healthy kidney tissue, and fat tissue.

The images in Fig.6.12 show the autofluorescence intensities measured by the three photomultiplier tubes without application of the OCSA-Transformation (equation 5.4). Nearly no contrast is visible in these pictures. However, Fig.6.14 nicely shows that after analysis with the OCSA (but no additional image processing, despite the 'normalization' mentioned above (in chapter 5.1)) the same images show much more contrast (Fig.6.13). Channel three (Fig.6.13(right)) shows a very low signal, thus illustrating that there is almost no reference tissue three (fat) present in the observed specimen, whereas the signals of channel one (carcinoma, Fig.6.13(left)) and channel two (healthy kidney, Fig.6.13(center)) can be clearly distinguished.

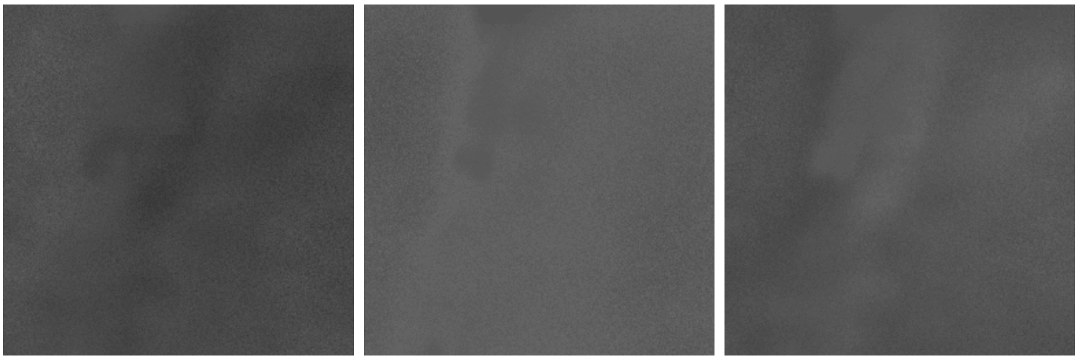

Figure 6.12: Autofluorescence signal of human tissue (transition between kidney and kidney carcinoma) measured by the three photomultiplier tubes which are shown separately (left: 450-500 *nm*; center: 500-550 *nm*; right: 550-600 *nm*). The excitation wavelength is 442 *nm*. Nearly no contrast is seen without any image enhancement.

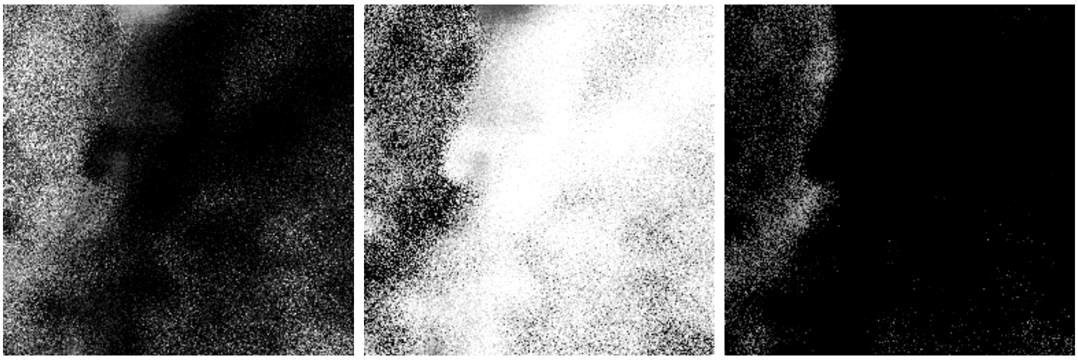

Figure 6.13: Images in the domain of the reference tissues (Fig.6.8 after analysis with the OCSA). Channel one (left) corresponds to carcinoma of the kidney and channel two (center) to healthy kidney tissue. The third channel (right) corresponds to fat tissue. These images show strong contrast, although there is nearly no contrast seen in the images taken without the OCSA-Transformation.

Most of the values are associated with healthy kidney tissue (value: 256), which corresponds to the real distribution in the sample.

So far only basic operations were applied to the obtained data: Two operations were applied to all vectors (measurement and calculation). First, all values smaller than zero were set to zero, in order to suppress errors of the PMT's amplifiers. In the second step, each vector value (corresponding to one point in the sample) was divided by the sum of the values of the vector. This operation was done in order to suppress the effect of intensity fluctuations of the measured results (Only the relative intensities are of interest). Strikingly, even

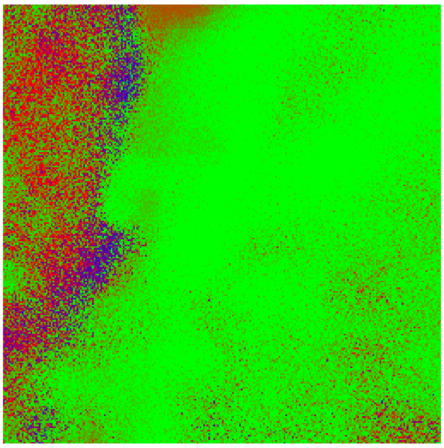

Figure 6.14: The images of Fig.6.13 are combined to a color coded image. Red corresponds to carcinoma, green to healthy kidney tissue and blue to fat tissue.

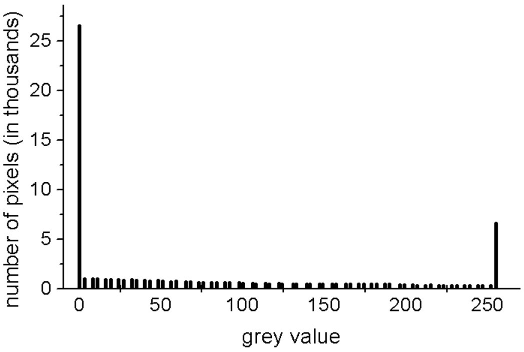

Figure 6.15: Histogram of the left half of Fig.6.13(center). Most of the pixels are either zero (in this case corresponding to carcinoma) or 256 (corresponding to healthy kidney).

with this simple method, very good results were obtained (see above). No image enhancement at all was applied to the images shown.

In the experiments described above it was possible to distinguish tissues in any given set of tissue triplets. Fig.6.15 shows a histogram of the left half of channel two (Fig.6.13(center)). This histogram shows, that most of the pixels were either zero (in this case corresponding to carcinoma) or 256 (corresponding to healthy kidney). No special optimization was done at this point, which could further increase image quality.

Chapter 7

Discussion and Conclusion

7.1 Discussion

Stereotactic laser neurosurgery is a recently developed method for resection of tumors from human brains. While conventional radiotherapy destroys relatively large areas of healthy brain tissue surrounding a tumor, stereotactic laser neurosurgery allows precise ablation of cancerous tissue without X-ray irradiation. However, the practical application of this method is at present associated with several problems and impediments. Thus, improvement of stereotactic laser neurosurgery is necessary because of the following reasons:

The precise delimitation of cancerous and healthy tissue is of high importance in order to prevent resection of healthy brain tissue. At present, the standard monitoring methods prior to and during an operation are CT and MR imaging methods, which show rather poor resolution. Additionally, these methods only deliver overall images from rather large brain sections but no detailed analysis of the actual point of interest during an operation. Thus, precise detection of various critical tissue types, e.g. blood vessels inside the brain is difficult when CT and MRI data are used as the only source of information. Real time imaging with CT and MRI is difficult due to the poor time resolution of these methods.

The aim of this work was planning, experimental design and application of a new analytic device which solves the above mentioned problems. One possibility to improve the reliability of detection of cancerous tissue in the brain is the use of fluorescent dyes. Several exogenous fluorescent dyes which were shown to specifically stain tumor tissue are known. However, their application is quite risky, as described in chapter 3.1. Since such fluorescent dyes specifically stain tumors, they do not allow mapping of other structures like blood vessels.

In contrast, this work was based on the idea of making use of the autofluorescence properties of cells. As described in chapter 3.3, it was shown before that it is possible to visualize and identify different types of tissues by analyzing their autofluorescence spectra. Many examples for cancer detection by fluorescent light, using the intrinsic autofluorescence properties of tissues, are given in literature [43, 68].

In order to make use of the relatively low autofluorescence intensities of tissues in the brain and to ensure the reliability of detection, a new and very sensitive analytic device, the OligoChannel Spectrum Analyzer (OCSA) was developed, realized for experimental applications and tested. With the OCSA, an analytic device with a more general approach was developed. Unlike in other methods it is less important to figure out an optimized combination of excitation and detection wavelengths with the OCSA, because the analysis of spectra is done by the multiplication with a matrix (OCSA-Transformation) obtained in the calibration process. This matrix itself is extracted from the spectral fingerprints of reference tissues and therefore includes all required information about the working configuration. During the process of calibration, three points in the brain are accessed. One point is chosen in healthy tissue on the path to the tumor, identified as healthy with the CT and MRI data. As a second point, a blood vessel is chosen. Finally, the third reference tissue measurement is taken inside the tumor volume before ablation starts. With these spectral fingerprints all information required for analysis is available.

Unfortunately, the natural fluorescence of cells, especially of brain tissue, is very low. Therefore, very long exposure times are necessary for detection with conventional OMAs. Such long exposure times are not tolerable in stereotactic brain surgery, since every point needs to be analyzed before ablation. Ablation of each point is done with a repetition rate of 4 kHz. This frequency cannot be reduced, since this would extend the duration of a surgery to a unacceptable length. OCSA meets the 4 kHz requirement due to its real time capability.

Our preliminary results nicely illustrate that it is possible to distinguish different types of tissue by examination with the OCSA (proof of principle). Each of the tissue triplets that were tested could be analyzed and the tissues could be classified with high reliability. Images obtained from autofluorescence measurements in mouse and human tissues provide information about the different fractions of reference tissues at any observed point of the specimen. Therefore, this new technique may provide an immediate light-biopsy diagnosis of cancer *in vivo*.

The goal of tissue sample preparation for our experiments was to keep as much of the *in vivo* properties of the tissue during measurements. Therefore, no conservation techniques were applied at all. In order to avoid changes of tissue properties, even cooling was avoided. It should be noted that, due to the relatively long durations of measurement, tissue properties might have changed during and between each measurement series. In the next step *in vivo* experiments could demonstrate the applicability of the method under real stereotactic conditions. In this context it is important to note that the dimensions of the apparatus, at least the part which is inserted into the patient´s head, do not increase when the OCSA is used. Thus, the use of the OCSA would not bring any disadvantages to the patient in terms of seriousness of an operation.

No additional optimization was done, like searching for suitable wavelengths. Both, excitation (442 nm) and detection (450-500-550 nm) wavelengths were fixed.

For optimization of the results, examination and detection wavelengths could be chosen individually for any given application. For example, good results were reported using laser light in the UV for applications in the brain [69]. But with the used setup (excitation 442 nm, detection 450-500-550 nm), a clear distinction between white and grey mouse brain matter was possible, indicating applicability of the used setup for stereotactic laser neurosurgery. Another possible enhancement may result from the use of a larger number of channels/detectors, as there are more than just three types of tissues present in the human brain. By using more than three channels a refined detection might be possible. Two or more channels can be associated with slightly different kinds of one type of tissue, allowing a tolerance in the detection.

The data can be analyzed and checked for plausibility, e.g. by matching adjacent pixels. It has to be evaluated whether there are parameters which allow a general use without the calibration process prior to each surgery.

The spatial resolution of the used setup is in the range of the ablated volumes and thus sufficient for the diagnosis of cancerous tissue during stereotactic neurosurgery. In a stereotactic laser neurosurgery setup the resolution is fixed by the properties of the lens in the periscopic probe tip. Since this lens is used for focusing the high energy laser beams as well as an imaging lens in the confocal setup, the resolution of detection is in the same range as the size of the ablated sample volume. This is sufficient in terms of analysis of the next sample volume of interest. Actually, the resolution is even better than that, since a confocal setup has an improved resolution (factor 1.4) compared to a conventional setup: the focused high energy laser beam can be seen as the illumination spot of a conventional scanning microscope (Fig.4.5(c)).

In addition, the laser used for diagnosis has a better beam quality (at least after spatial filtering in the beam expander) than the high energy lasers, leading to a smaller spot size and therefore higher resolution. The detection of fluorescent dyes in stereotactic neurosurgery, via a confocal microscope integrated in the optical probe, was evaluated by Zenzinger et al. [37]. *In vitro* experiments with the actual optical setup were performed [33].

The spatial resolution mainly depends on the optical setup of the confocal microscope in which the OCSA is used as a point detector. Therefore it can be easily adapted to a given problem (desired resolution) by changing the optical setup of the confocal microscope, including the detection/entrance pinhole of the OCSA.

Ensuring precise detection is necessary in order to make use of the precise plasma-induced ablation. However, it might be an advantage to induce thermal damage to parts of the tissue in order to stimulate the immune system to work against some possible residual tumor tissue and metastases. It is reported that after thermal treatment of a tumor, remaining tumor tissue and even metastases are eliminated by the immune system. Therefore, this additional stimulus, e.g. by heat induced damages induced with the coagulation system, might be useful to completely eliminate the cancer.

During an operation, the results received with the OCSA can be used for precise navigation, whereas the images obtained from CT/MRI (resolution in the *mm*-range) may be used for rough navigation. As the geometry in the human skull changes due to displacements of the brain when tumor volume is ablated, the online control with OCSA (in addition to the online MRI control, during the surgery an open MRI device can be used to improve access to the patient's skull) increases the precision of the tumor resection significantly.

The excitation wavelength reflected by the beam splitter BS3 (Fig.5.3) can be analyzed by a point detector in order to obtain pictures in the reflection mode (not used in the experiments described in this work). This may provide additional imaging information. The value of this information has to be evaluated for a given application.

To fulfil the need of MR compatibility, a fiber optic laser scanning microscope can be used. The fiber serves as a point source and point detector in the setup [70]. A main advantage of this would be that the detectors could be placed away from the high B-field of the MRI device

7.2 Conclusion

With the new OCSA direct information about the constituents of the observed tissue is obtained by analyzing its autofluorescence spectrum. With the use of just a few channels it is possible to acquire data with high sensitivity and speed. All data are sent to the computer simultaneously. The only general limitations are the read-out speed of the PMTs and the number of emitted photons. By using more than just the overall fluorescence intensity additional information is obtained. By transforming data with the new OCSA-method (OCSA-Transformation) tissue types can be identified. With this information the ablation process is controlled in order to remove cancerous tissue selectively and with high precision.

As there are some optimization possibilities available (larger amount of channels, better detectors, specialized setup for a given application, matching of adjacent points for plausibility check, etc.), there should exist a working setup of the OCSA for any given application.

Additionally, there might be various possible application areas in diagnostics. For every application, with three or more channels, like e.g. a confocal scanning microscope, this algorithm (OCSA-Transformation) can be implemented to receive additional information about the observed object.

Appendix A

Adaptive Optics

Adaptive Optics (AO) is used to correct optical aberrations in an optical system induced by changes in the refractive properties of optical elements. It is a widely used technique in astronomy. Imperfect optical elements are e.g. the atmosphere in case of astronomy, or in case of stereotactic neurosurgery, the biological sample and the irrigation liquid which have to be passed by the beam in order to get to the imaged part of the sample.

As in confocal microscopes the samples are imaged point by point, there is no need to correct several planes in order to correct all aberrations like in astronomy. In astronomy, the wavefront is sensed by using a bright star or a laser beacon (laser guide star). The correction is valid for the area around the beacon and in a specific layer in the atmosphere only. The corrective element is in a corresponding layer to a layer in the atmosphere. Only the turbulences in this layer are completely corrected. For a better correction, a multilayer adaptive optic system has to be used. A transition to many layers leads to a tomographic access. That means that the turbulences in the whole passed atmospheric space are measured and corrected. The consequence is an immense increase in system complexity.

A.1 Adaptive Optics in Stereotactic Laser Neurosurgery

In Fig.A.1 a system overview of an AO stereotactic laser neurosurgery setup is given. One part is the spectrometer and OCSA section analyzing the observed point and controlling the lasers for ablation and coagulation.

The second control loop in this setup is the AO system. It consists of a Hartmann-Shack Sensor (HSS) analyzing the wavefront and an actuator correcting the aberrated wavefront. The analysis of the data delivered by the HSS and the control of the actuator is done with a regular computer. The system has to work in real time. At the moment the used HSS (with ASIC detector, see chapter A.2.1) and mirror (membrane mirror, see chapter A.3) are limited to a frequency of about 500 Hz. Further research is necessary to meet the 4 kHz requirement for the use in stereotactic laser neurosurgery. The position of the actuator (corrective element) is chosen in order to correct the distortion of the microscope signal and to pre-correct the high energy laser beams.

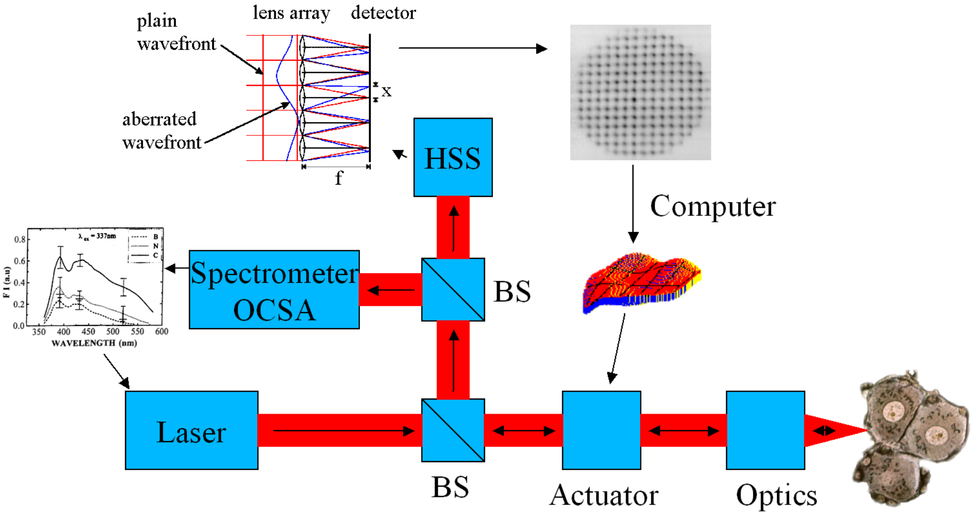

Figure A.1: System overview of an adaptive confocal fluorescence microscope for stereotactic neurosurgery. [71]. (BS: beam splitter, HSS: Hartmann-Shack sensor).

A.2 Wavefront sensing

The propagation of light can be described with wavefronts, which are planes of equal phase. These wavefronts are perpendicular to the rays used in geometric optics. In this work only Hartmann-Shack sensors (HSS) in combination with a membrane mirror are described in detail.

A.2.1 The Hartmann-Shack wavefront sensor

The wavefront can be measured with a Hartmann-Shack wavefront sensor (HSS). Its basic principle was invented by Hartmann for quality testing of telescopes. In the first setup, a parallel beam was incident on an array of pinholes. The tested lens behind the pinhole-array focused the light. In two planes before and behind the focal plane images were taken. With an ideal lens corresponding points on the two images are in corresponding positions. With an imperfect lens, the points are displaced and the aberrations can be analyzed.

In 1971, Shack refined this principle by replacing the pinhole-plate by an array of small lenses. Each lens samples a small part of the wavefront. The displacement of a focal point of one lens represents the averaged tilt of the wavefront in the area of the lens. Parallel light with a small angle of incidence to a lens is focused onto the focal plane, but with a displacement from the optical axis (Fig.A.2 left).

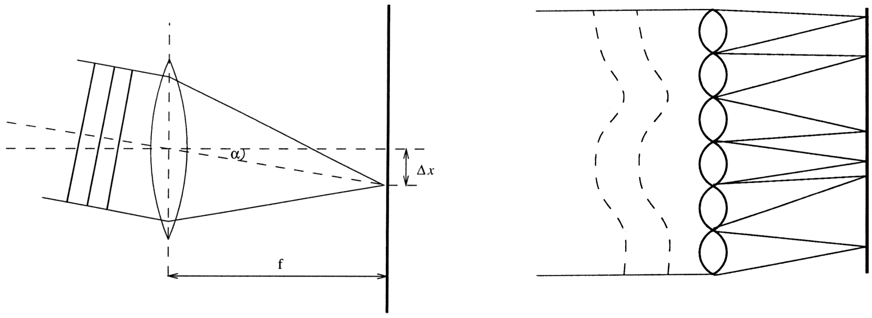

Figure A.2: left: Displacement of the focal point of a lens. right: Hartmann-Shack sensor.

The displacement is:

$$\Delta x = f \times \tan \alpha \tag{A.1}$$

A Hartmann-Shack sensor (HSS) consists of a microlens-array and a CCD device for imaging. The image on the CCD-device is digitized by a frame-grabber in a computer and analyzed.

For real time applications, the use of a CCD-device in combination with a frame-grabber is often too slow. Therefore an Application Specific Integrated Circuit (ASIC) is developed [72]. This microchip combines a detector array and some of the analytic circuits. Detection rates in the kHz-range are possible.

A.2.2 Wavefront reconstruction

The slope of the wavefront is measured at several points with the HSS. At N points, corresponding to the centers of the lenses, the slope of the wavefront is known. i gives the number of one element (lens).

$$\frac{\partial W(x_i, y_i)}{\partial x} = \frac{\Delta x_i}{f} \tag{A.2}$$

$$\frac{\partial W(x_i, y_i)}{\partial y} = \frac{\Delta y_i}{f} \tag{A.3}$$

This equation can be solved with a wavefront built from orthogonal polynomials L_i. M is the maximal rank of the polynomials:

$$\frac{\partial W_T(x, y)}{\partial x} = \sum_{i=1}^{M} k_i L_i(x, y) \tag{A.4}$$

$$\frac{\partial W_T(x,y)}{\partial y} = \sum_{i=1}^{M} l_i L_i(x,y) \tag{A.5}$$

For the criterion of the fit the method of least square fit is used: The square of the deviation S between the wavefront derivative and the measured derivative for x and y has to be minimal:

$$S = \sum_{i=1}^{N} \left(\left(\frac{\Delta x_n}{f} - \frac{\partial W_T(x_n,y_n)}{\partial x} \right)^2 + \left(\frac{\Delta y_n}{f} - \frac{\partial W_T(x_n,y_n)}{\partial y} \right)^2 \right) \tag{A.6}$$

With equation A.4 we get:

$$S = \sum_{i=1}^{N} \left(\left(\frac{\Delta x_n}{f} - \sum_{i=1}^{M} k_i L_i(x_n,y_n) \right)^2 + \left(\frac{\Delta y_n}{f} - \sum_{i=1}^{M} l_i L_i(x_n,y_n) \right)^2 \right) \tag{A.7}$$

The sum is minimal for:

$$0 = \frac{\partial S}{\partial k_j} = \sum_{n=1}^{N} \sum_{i=1}^{M} \left(k_i L_i(x_n,y_n) - \frac{\Delta x_n}{f} \right) L_j(x_n,y_n) \tag{A.8}$$

$$0 = \frac{\partial S}{\partial l_j} = \sum_{n=1}^{N} \sum_{i=1}^{M} \left(l_i L_i(x_n,y_n) - \frac{\Delta y_n}{f} \right) L_j(x_n,y_n) \tag{A.9}$$

This can be transformed:

$$\sum_{n=1}^{N} \frac{\Delta x_n}{f} L_j(x_n,y_n) = \sum_{i=1}^{M} k_i \sum_{n=1}^{N} L_i(x_n,y_n) L_j(x_n,y_n) \tag{A.10}$$

$$\sum_{n=1}^{N} \frac{\Delta y_n}{f} L_j(x_n,y_n) = \sum_{i=1}^{M} l_i \sum_{n=1}^{N} L_i(x_n,y_n) L_j(x_n,y_n) \tag{A.11}$$

For orthogonal polynomials (they have to be normalized for the given detector geometry) with $i \neq j$:

$$\sum_{n=1}^{N} L_i(x_n,y_n) L_j(x_n,y_n) = 0, \tag{A.12}$$

These can be solved to get k_i and l_i

$$k_i = \frac{\sum_{n=1}^{N} \frac{\Delta x_n}{f} L_j(x_n, y_n)}{\sum_{n=1}^{N} L_i(x_n, y_n)^2} \tag{A.13}$$

$$l_i = \frac{\sum_{n=1}^{N} \frac{\Delta y_n}{f} L_j(x_n, y_n)}{\sum_{n=1}^{N} L_i(x_n, y_n)^2} \tag{A.14}$$

By comparison of the coefficients the so-called Zernike polynomials are obtained.

A.2.3 Zernike polynomials

The polynomials were introduced by Zernike in 1934 to describe aberrations in spherical mirrors. The polynomials are orthonormal over a circle with diameter one. The polynomials represent classical aberrations. In table A.1 the first 15 polynomials (up to the fourth rank) are listed.

Rank		mononom-notation	name
0	Z_0	1	constant
1	Z_1	x	x-tilt
	Z_2	y	y-tilt
2	Z_3	$2xy$	astigmatism ±45°
	Z_4	$2x^2 + 2y^2 - 1$	defocus
	Z_5	$y^2 - x^2$	astigmatism 0°/90°
3	Z_6	$3xy^2 - x^3$	
	Z_7	$-2x + 3xy^2 + 3^3$	x-coma
	Z_8	$-2y + 3x^2y + 3y^3$	y-coma
	Z_9	$y^3 - 3x^2y$	
4	Z_{10}	$4y^3x - 4x^3y$	
	Z_{11}	$-6xy + 8y^3x + 8x^3y$	
	Z_{12}	$1 - 6y^2 - 6x^2 + 6y^4 + 12x^2y^2 + 6x^4$	spherical aberration
	Z_{13}	$-3y^2 + 3x^2 + 4y^4 - 4x^4$	
	Z_{14}	$y^4 - 6x^2y^2 + 4x^4$	

Table A.1: Zernike-polynomials in the notation of Malacara.

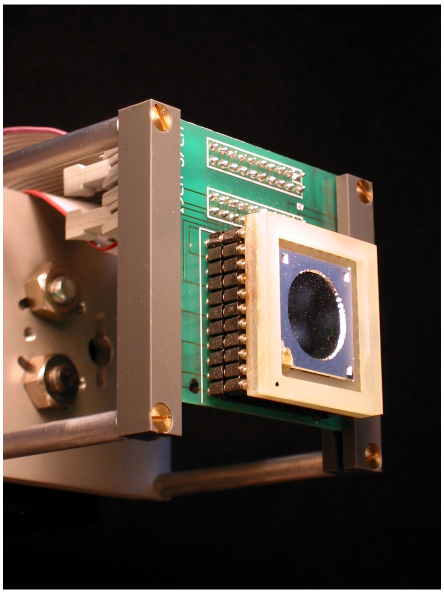

Figure A.3: Membrane mirror mount mounted onto a circuit board with connecting cables.

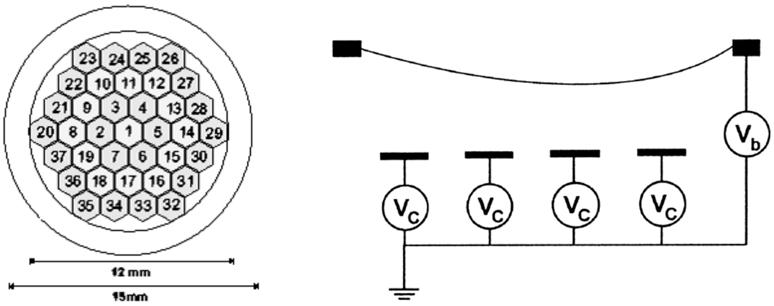

Figure A.4: Schematic drawing of the structure of a membrane-mirror.

A.3 Membrane mirror

For the correction of the wavefront a membrane-mirror from Oko Technologies (Netherlands) was used (Fig.A.3). 37 hexagonal electrodes are arranged underneath the membrane. Dependent on the voltages applied to the elements, the form of the mirror is changed. Structure and setup of the mirror are schematically shown in Fig.A.4. Fig.A.5 shows the measured mirror surface with applied voltages to element 1 (left) and to element 2 (right). The measurements are obtained with an Twyman-Green interferometer (Fisba optic, Switzerland).

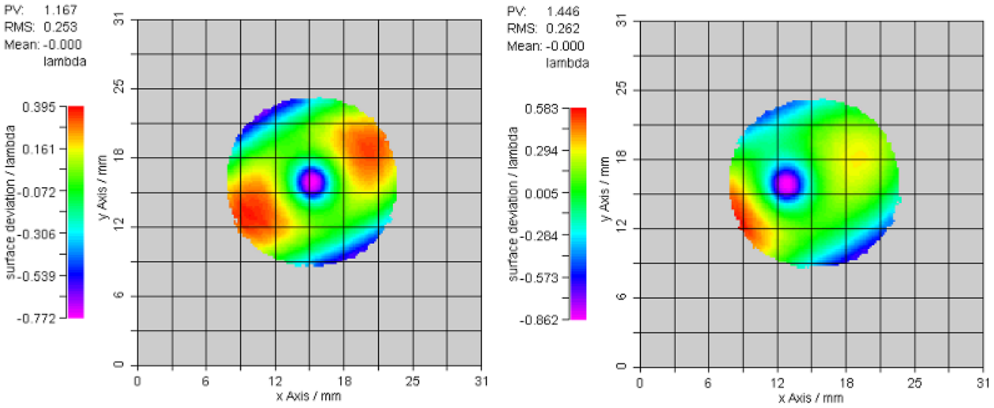

Figure A.5: Interferometric images of the mirror surface. left: Voltage applied at element 1. right: Voltage applied at element 2.

A.4 Curvature sensing

Roddier et al. described a method called *curvature sensing* for wavefront sensing [73]. The wavefront is focused by a lens. By comparing two irradiance distributions at equally spaced points on either side of the focal plane, the local curvature (second derivative) is obtained.

An advantage of this technique is, that a correction can be applied without the intermediate step of wavefront reconstruction. Some correction devices, especially bimorph mirrors, can locally deform into near-spherical shape. If the sensor subapertures and the corrector actuators are aligned, a very efficient process for wavefront sensing is the result.

A.5 Bimorph mirror

A deformable *bimorph mirror* consists of a glass or metal frontplate bonded to a piezoelectric ceramic. The interface glued between the frontplate and the ceramic contains a conducting electrode. The back of the ceramic is covered with a number (matching the geometry of the detector) of electrodes. The front surface is polished to form the reflective surface of the deformable mirror. If a voltage is applied between the front electrode and one of the electrodes at the back, the ceramic changes in size and a curvature is induced on the surface.

A.6 Segmented mirror

Segmented mirrors are made of a number of small mirror elements with piston or tilt capability. Piston mirrors can only perform up-and-down movement, changing the phase of a reflelcted wavefront. In piston-tilt mirrors each element can additionally perform a tilt movement in the x and y direction.

A.7 The liquid crystal spatial light modulator

A liquid crystal spatial light modulator (SLM) is a compact low-cost alternative to deformable mirrors [74]. The refractive index of the material and therefore the optical pathlength is changed. To act as a piston-only segmented deformable mirror the SLM has to be used with polarized light. SLMs can be used in transmission, which can be useful in some applications.

Bibliography

[1] K. Greger, J. Bille, W. Schlegel, V. Sturm, *Stereotaktische Laser-Neurochirurgie*, Medizinische Physik (editors: J. Bille, W. Schlegel), Band 3, Springer, in press.

[2] N. Suhm, M.H. Goetz, J.P. Fischer, F. Loesel, W. Schlegel, V. Sturm, J.F. Bille, R. Schröder, *Ablation of Neural Tissue by Short-Pulsed Lasers - a Technical Report*, Acta Neurochir. (Wien) **138**, 346-349 (1996).

[3] J. Bille, W. Schlegel, *Medizinische Physik*. Band 2, Springer (1999).

[4] K. Greger: *Aufbau eines konfokalen Laser-Scanning-Mikroskops mit hoher Bildwiederholfrequenz zur minimal invasiven Tumordiagnostik.* Diploma thesis, Fakultät für Physik, University of Ulm (2000).

[5] T. Wilson, C. Sheppard, *Theory and Practice of Scanning Optical Microscopy*, Academic Press (1984).

[6] M. Minsky, *U.S. Patent 3013467: Microscopy Apparatus*, Dec. 19, 1961, (Filed Nov. 7, 1957).

[7] J.B. Pawley (Editor): *Handbook of Biological Confocal Microscopy*, Plenum Press (1995).

[8] C. Smithpeter, A. Dunn, R. Drezek, T. Collier, R. Richards-Kortum, *Near real time confocal microscopy of cultured amelanotic cells: sources of signal, contrast agents and limits of contrast*, Journal of Biomedical Optics **3(4)**, 429-436 (1998).

[9] M. Rajadhyaksha, R.R. Anderson, R.H. Webb, *Video-rate confocal scanning laser microscope for imaging human tissues in vivo*, Applied Optics **38(10)** 2105-2115 (1999).

[10] M. Kriegmair, D. Zaak, K.-H. Tothenberger, J. Rassweiler, D. Jocham, F. Eisenberger, R. Tauber, A. Stenzl, A. Hofstetter, *Transurethal resection for bladder cancer using 5-aminolevulinic acid induced fluorescence endoscopy versus white light endoscopy*, The Journal of Urology **168**, 475-478 (2002).

[11] O.A. Gederaas, A. Holroyd, S.B. Brown, D. Vernon, J. Moan, K. Berg, *5-Aminolaevulinic acid methyl ester transport on amino acid carriers in a human colon adenocarcinoma cell line*, Photochemistry and Photobiology **73(2)**, 164-169 (2001).

[12] J.T.H.M. van den Akker, V. Iani, W.M. Star, H.J.C.M. Sterenborg, J. Moran, *Systemic component of Protoporphyrin IX production in nude mouse skin upon topical application of Aminolevulinic Acid depends on the application conditions*, Photochemistry and Photobiology **75(2)**, 172-177 (2002).

[13] W.S. Poon, K.T. Schomacker, T.F. Deutsch, R.L. Martuza, *Laser-induced fluorescence: experimental intraoperative delineation of tumor resection margins*, J. Neurosurg. **76**, 679-686 (1992).

[14] R. Richards-Kortum, E. Sevick-Muraca, *Quantitative optical spectroscopy for tissue diagnosis*, Annu. Rev. Phys. Chem. **47**, 555-606 (1996).

[15] A.J. Welch, C. Gardner, R. Richards-Kortum, E. Chan, G. Criswell, J. Pfefer, S. Warren, *Propagation of fluorescent light*, Laser in Surgery and Medicine **21**, 166-178 (1997).

[16] L. Rigacci, R. Alterini, P.A. Bernabei, P.R. Ferrini, G. Agati, F. Fusi, M. Monici, *Multispectral imaging autofluorescence microscopy for the analysis of lymph-node tissues*, Photochemistry and Photobiology **71(6)**, 737-742 (2000).

[17] R. Drezek, C. Brookner, I. Pavlova, I. Boiko, A. Malpica, R. Lotan, M. Follen, R. Richards-Kortum, *Autofluorescence microscopy of fresh cervical-tissue sections reveals alterations in tissue biochemistry with dysplasia*, Photochemistry and Photobiology **73(6)**, 636-641 (2001).

[18] C.S. Betz, M. Mehlmann, K. Rick, H. Stepp, G. Grevers, R. Baumgartner, A. Leunig, *Autofluorescence imaging and spectroscopy of normal and malignant mucosa in patients with head and neck cancer*, Laser in Surgery and Medicine **25**, 323-334 (1999).

[19] B.W. Chwirot, S. Chwirot, W. Jerzejczyk, M. Jackowski, A.M. Raczynska, J. Winczakiewicz, J. Dobber, *Ultraviolet laser-induced fluorescence of human stomach tissues: Detection of cancer tissues by imaging techniques*, Laser in Surgery and Medicine **21**, 149-158 (1997).

[20] D.L. Heintzelman, R. Lotan, R. Richards-Kortum, *Characterization of the autofluorescence of polymorphonuclear leukocytes, mononuclear leukocytes and cervical epithelial cancer cells for improved spectroscopic discrimination of inflammation from dysplasia*, Photochemistry and Photobiology **71(3)**, 327-332 (2000).

[21] C. Brookner, M. Follen, I. Boiko, J. Galvan, S. Thomsen, A. Malpica, S. Suzuki, R. Lotan, R. Richards-Kortum, *Autofluorescence patterns in short-term cultures of normal cervical tissue*, Photochemistry and Photobiology **71(6)**, 730-736 (2001).

[22] L. Brancaleon, A.J. Durkin, J.H. Tu, G. Menaker, J.D. Fallon, N. Kollias, *In vivo fluorescence spectroscopy of nonmelanoma skin cancer*, Photochemistry and Photobiology **73(2)**, 178-183 (2001).

[23] Y.P. Sinichkin, S.R. Utz, A.H. Mavliutov, H.A. Pilipenko, *In vivo fluorescence spectroscopy of the human skin: Experiments and models*, Journal of Biomedical Optics **3(2)**, 201-211 (1998).

[24] H. Zeng, C. MacAulay, D.I. McLean, B. Palcic, *Spectroscopic and microscopic characteristics of human skin autofluorescence emission*, Photochemistry and Photobiology **61(6)**, 639-645 (1995).

[25] M. Kobayashi, K. Shibuya, H. Hoshino, T. Fujisawa, *Spectroscopic analysis of the autofluorescence from human bronchus using an ultraviolet laser diode*, Journal of Biomedical Optics **7(4)**, 603-608 (2002).

[26] M. Anidjar, O. Cussenot, S. Avrillier, D. Ettori, J.M. Villette, J. Fiet, P. Teillac, A. Le Due, *Ultraviolet laser-induced autofluorescence distinction between malignant and normal urothelial cells and tissues*, Journal of Biomedical Optics **1(3)**, 335-341 (1996).

[27] R.R. Alfano et al., *Fluorescence Spectra from Cancerous and Normal Human Breast and Lung Tissue*, IEEE J. of Quantum Electronics **QE-23**, No. 10 (Oct. 1987).

[28] G. Divkovic, *Aufbau eines konfokalen Fluoreszenzmikroskops zur Gewebediagnose*, Diploma thesis, University of Heidelberg (2001).

[29] W. Schlegel, V. Sturm, *Computer application systems in radiation therapy and stereotactic neurosurgery*, H.U. Lemke (Hrsg.), Meical Imaging and Computer Assisted Radiology, 107, CAR-Tutorial, Technische Universität Berlin (1991).

[30] K. Poeck, *Neurologie*, 9. Auflage, Springer-Verlag (1994).

[31] International Commission on Radiation Units and Measurements (ICRU), *Prescribing, Recording and Reporting Photon Beam Therapy*, ICRU Report 50, Washington (1993).

[32] A. Pirzkall, M. Carol, F. Lohr, A. Höss, M. Wannenmacher, J. Debus, *Comparison of intensity-modulated radiotherapy with conventional conformal radiotherapy for complex-shaped tumors*, Int. J. Radiation Oncology Biol. Phys. **48**, 1371-1380 (2000).

[33] M.H. Goetz, S.K. Fischer, A. Velten, J.F. Bille, V. Sturm, *Computer-guided laser probe for ablation of brain tumors with ultrashort laser pulses*, Phys. Med. Biol. **44**, 119-127 (1999).

[34] J. Wahrburg, K. Schmidt, M.H. Götz, K. Kappings, S. Gölz, *Concept of a novel laser probe for minimal invasive applications in neurosurgery*, Mechatronics Vol. 6, No. 4 479-489 (1996).

[35] J. Wolf, *Spektroskopie von Pikosekunden-Laserpulsen auf Hirngewebe und Untersuchung von Laser-Koagulation zur Kontrolle eines neurochirurgischen Eingriffs*, Diploma thesis, University of Heidelberg (1997).

[36] K. Sultan, *Entwicklung eines druckgeregelten Spülsystems für Anwendungen in der Neurochirurgie*, Dissertation, University of Heidelberg (2000).

[37] M. Zenzinger, M.H. Götz, S. Fischer, J. Bille, *Confocal fluorescence microscopy for minimal-invasive tumor diagnosis*, Appl. Phys. B **70**, 281-286 (2000).

[38] J.R. Lakowicz, *Principles of fluorescence spectroscopy*, Plenum Press, New York (1984).

[39] W. Demtröder, *Laser Spectroscopy: Basic concepts and instrumentation*, Springer-Verlag (1998).

[40] F.W.D. Rost, *Quantitative Fluorescence Microscopy*, Cambridge University Press, Cambridge, UK (1991).

[41] R.R. Alfano, *Laser induced fluorescence spectroscopy from native cancerous and normal tissue*, IEEE J. Quant. Electron. **20**, 1507-1511 (1984).

[42] M. Kriegmair, R. Baumgartner, W. Lumper, R. Riesenberg, S. Stocker, A. Hofstetter, *Fluorescence cystoscopy following intravesical instillation of 5-aminolevulinic acid (ALA)*, The Journal of Urology **149**, 240 (1993).

[43] G.A. Wagnieres, W.M. Star, B.C. Wilson, *In vivo fluorescence spectroscopy and imaging for oncological applications*, Photochemistry and Photobiology **68(5)**, 603-632 (1998).

[44] W. Kuehne, *Taschenbuch der Zytologie, Histologie und mikroskopischen Anatomie*, 8. Auflage, Thieme (1992).

[45] R.C. Mellors, A. Glassman, G.N. Papanicolaou, *A microfluorometric scanning method for the detection of cancer cells in smears of exfoliated cells*, Cancer, **5**, 458-468 (1952).

[46] S. Lam, B. Palcic, D. McLean, J. Hung, M. Korbelik, A.E. Profio, *Detection of early lung cancer using low dose Photofrin II*, Chest **97**, 333-337 (1990).

[47] S. Anderson-Engels, C. af Klinteberg, K. Svanberg, S. Svanberg, *In vivo fluorescence imaging for tissue diagnosis*, Phys. Med. Biol. **42**, 815-824 (1997).

[48] I.J. Bigio, J.R. Mourant, *Ultraviolet and visible spectroscopies for tissue diagnostics: fluorescence spectroscopy and elastic scattering spectroscopy*, Phys. Med. Biol. **42**, 803-814 (1997).

[49] Q. Peng, K. Berg, J. Moan, M. Kongshaug, J.M. Nesland, *5-Aminolevulinic acid-based photodynamic therapy - principles and experimental research*, Photochemistry and Photobiology **65(2)**, 235-251 (1997).

[50] H.A. Dailey, A. Smith, *Differential interaction of porphyrins used in photoradiation therapy with ferrochelatase*, Biochemical Journal **223**, 441-445 (1984).

[51] R. Van Hillenberg, J.M. Van den Berg, W.J. Kort, O.T. Terpstra, J.H. Wilson, *Selective accumulation of endogenously produced porphirins in a liver matastasis model in rats*, Gastronterology **103(2)**, 647-651 (1992).

[52] C. Gerthsen, H.O. Kneser, H. Vogel: *Physik*. 16. Auflage, Springer-Verlag (1992).

[53] S.K. Fischer, *Entwicklung eines konfokalen Laserscanning-Mikroskops zum Einsatz in der stereotaktischen Laser-Neurochirurgie*, Dissertation, University of Heidelberg (1996).

[54] M. Zenzinger: *Aufbau eines konfokalen Fluoreszenz-Mikroskops zur minimalinvasiven Tumordiagnostik in der Laser-Neurochirurgie*, Diploma thesis, University of Heidelberg (1998).

[55] J.-L. Boulnois, *Photophysical processes in recent medical laser development: a review*, Lasers in Medical Science **1**, 47-66 (1986).

[56] M.H. Niemz, *Lasers-Tissue Interaction*, Springer-Verlag, Berlin, Heidelberg (1996).

[57] F.A. Duck, *Physical properties of tissue*, Academic Press, London (1990).

[58] W. Koechner, *Solid-state laser engineering*, Springer-Verlag (1999).

[59] A. Velten, *Anwendungen von Pikosekunden- und Dauerstrichlasern mit hoher Ausgangsleistung in der stereotaktischen Neurochirurgie*, Dissertation, University of Heidelberg (2000).

[60] M. Young: *Optik, Laser, Wellenleiter*, Springer-Verlag (1997).

[61] R. Nitzmann, *Entwicklung und Bau einer automatischen Laserstrahljustierung für ein Operationssytem in der stereotaktischen Laser-Neurochirurgie*, Diploma thesis, University of Heidelberg (1999).

[62] http://www.trolltech.com/products/qt/index.html: *QT class library*, Trolltech AS, Oslo, Norway.

[63] W.T. Vetterling, S.A. Teukolsky, W.H. Press, B.P. Flannery, *Numerical recipies in C* (second edition), Cambridge university press (1992).

[64] K. Greger, J. Bille, *OligoChannel Spectral Analysis in Stereotactic Neurosurgery*, IFMBE Proc, **3(2)** 1566-1567 (2002).

[65] K. Greger, J. Bille, *OligoChannel Spectral Analysis, a new autofluorescence-based method for diagnosis of cancer in human brain tissue during stereotactic laser neurosurgery*, Journal of Biomedical Optics, to be published (2003).

[66] K. Greger, J. Bille, *OligoChannel Spectral Analyse in der Stereotaktischen Neurochirurgie*, Conference CD, DGMP-conference Gmunden, **506** (2002).

[67] B. Honig, *Theoretical aspects of photoisomerization*, in Biological Events Probed by Ultrafast Laser Spectroscopy, R.R. Alfano, Ed. New York: Academic, 285 (1982).

[68] P. Kremer, A. Wunder, H. Sinn, T. Haase, M. Rheinwald, U. Zillmann, F.K. Albert, S. Kunze, *Laser-induced fluorescence detection of malignant gliomas using fluorescein-labeled serum albumin: Experimental and preliminary clinical results*, Neurological Research **22**, 481-489 (2000).

[69] W.-C. Lin, S.A. Toms, M. Johnson, E.D. Jansen, A. Mahadevan-Jansen, *In vivo brain tumor demarcation using optical spectroscopy*, Photochemistry and Photobiology **73(4)**, 396-402 (2001).

[70] P.M. Delaney, M.R. Harris, R.G. King, *Fiber-optic laser scanning confocal microscope suitable for fluorescence imaging*, Applied Optics **33**, No. 4, 573-577 (1994).

[71] K. Greger, G. Divkovic, J. Bille, *Adaptiv Konfokale Fluoreszenzmikroskopie in der Minimal Invasiven Laserneurochirurgie*, Medizinische Physik 2001 (Herausg. K. Welker), 359-360 (2001).

[72] T. Nirmaier, D. Droste, J. Bille, *Hartmann-Shack sensor ASICs for real-time adaptive optics in biomedical physics*, The 6th multiconference on systemics, Vol. 13, 280-284 (2002).

[73] F. Roddier, *Curvature sensing and compensation: a new concept in adaptive optics*, Appl. Opt., **27**, 1223 (1988).

[74] J. Gonglewski, S. Browne, S. Rogers, S. McDermott *Adaptive optics using liquid crystal phase modulator in conjunction with a shack-hartmann wave-front sensor and zonal control algorithm*, Optics Express, **1(11)**, 338-346 (1997).

List of Figures

List of Tables

Acknowledgments

Special Thanks to:

- Prof. Dr. Josef Bille for the possibility to work on the interesting topics of medical physics and oncology.
- Prof. Dr. Wolfgang Schlegel for his interest in my work and for agreeing to be the second referee.
- Thorsten Liebler for his help with programming problems and for his constant support.
- Lars Hildenbrand for the interesting discussions and his good ideas.
- Lisa Kierig for the good time in the lab.
- Gabriela Divkovic for the good collaboration.
- Dr. Gernot Kuhr for his helpful remarks.
- All the people from the lab for the unique working conditions.
- Dr. Andreas Velten and the other people from MRC Systems for their help.
- Sonja Welsch for her patience.

Special thanks to my parents, who always supported me and made this possible, especially my father to whom I want to dedicate this work.